IEEE Access
Multidisciplinary | Rapid Review | Open Access Journal

Received 6 October 2022, accepted 17 October 2022, date of publication 21 October 2022, date of current version 31 October 2022.

Digital Object Identifier 10.1109/ACCESS.2022.3216296

SURVEY

Sensor-Based Ore Sorting–A Review of Current Use of Electromagnetic Spectrum in Sorting

ERNEST GOMOLEMO MODISE[1], (Member, IEEE), ADAMU MURTALA ZUNGERU[1], (Senior Member, IEEE), BOKANI MTENGI[1], (Member, IEEE), AND ALBERT UCHENNA UDE[2]

[1]Department of Electrical, Computer and Telecommunications Engineering, Botswana International University of Science and Technology, Palapye 10071, Botswana

[2]Department of Mechanical, Energy and Industrial Engineering, Botswana International University of Science and Technology, Palapye 10071, Botswana

Corresponding authors: Adamu Murtala Zungeru (zungerum@biust.ac.bw) and Ernest Gomolemo Modise (me19100032@studentmail.biust.ac.bw)

This work was supported by the Office of Research, Development, and Innovation (ORDI) of the Botswana International University of Science and Technology under Grant R00073.

ABSTRACT Sensor-based sorting has had a wide range of industrial use in automating and speeding up the process which requires substances or objects to be segregated from each other. The high demand for goods including raw materials, food, minerals, and waste recycling has increased the pressure for high-speed sorting. The first part of this paper presents a comprehensive theoretical and practical survey and comparison of current sorting methods relying on the use of the electromagnetic spectrum. Sorting methods are classified among other things, which portion of the EM spectrum is it, background noise rejection capacity, sample size limitations, sample chemistry limitations, sample surface cleanliness, spatial resolution capacity, spectral resolution, and feed rate limitations. The analysis focuses on color or visible light sorting, gamma-ray sorting, infra-red sorting, x-ray transmission-based sorting and x-ray fluorescence sorting, coupling the findings to the classification criteria outlined. We see a need to define a universal sorting scheme that will in general be applied to most sorting tasks. To do this, the final part of this paper re-looks at the x-ray transmission and x-ray fluorescence sorting scheme in line with the established limitations and proposes a dual x-ray transmission and fluorescence method to mitigate the challenge affecting the different schemes.

INDEX TERMS Albedo, bidirectional reflectance, color classification, detectability, gamma-ray spectroscopy, infrared spectroscopy, sorting, x-ray fluorescence, x-ray luminescence, x-ray self-absorption, x-ray transmission spectroscopy.

I. INTRODUCTION

The Sensor based ore sorting is the application of the interaction of matter with different portions of the electromagnetic (EM) spectrum in much similar process flow as the human vision system, to effect discrimination between samples, objects, or substances. The general sensor-based ore sorting infrastructure consists of a sample, a source of EM waves, interaction in the form of scattering, an EM sensing device, an interpreter, and an electro-mechanical classifying agent. The sensing element transforms the collected EM waves to an equivalent electrical signal generally proportional to the intensity of the EM wave incident on it. The incident wave scattered from the sample of interest can carry surface, boundary or internal properties of the material which are relevant features for classification. Non-penetrative EM waves rely on material reflectance properties while penetrative waves exploit the uniqueness of transmission resistance material properties. In all the use cases, a calibration criterion is used to set detection thresholds as a function of the intensity of the EM wave captured by the sensing pixel.

The associate editor coordinating the review of this manuscript and approving it for publication was Norbert Herencsar.

The decrease in ore grades and high beneficiation cost has fueled the miner's appetite to consider sensor-based ore sorting as a key driver in throughput increase and cost reduction measures. Such interest has motivated intensive research in the space of sensor base ore sorting focusing on detection efficiency and speed. Sensor-based ore sorting has been used in various mineral applications including diamonds, gold, copper, coal, lignite, hematite, quartz and many other minerals of value. Recently some review articles have published in the same area [1], [2], [3], [4], [5], [6], [7], [8], [9], [10], [11], [12], [13], [14], [15], [16], [17], [18], [19], [20] creating an exchange platform for cost effective engineering solutions in sensor based ore sorting. More beneficiation and advanced techniques for minerals like copper, coal, and diamond have also been proposed in [21], [22], [23], [24], [25], [26], [27], [28], [29], [30], [31], [32], [33], [34], [35], and [36], but none of these approaches intently reviews a generalized approach to sensor based ore sorting through the application of the interaction of electromagnetic waves with matter.

Sensor-based sorting or classification of substances is a five-step process involving the scattering of an EM wave from a sample, collection of the scattered wave by a sensing device, transduction to an electrical signal, comparing of the measured signal to a predetermined threshold and an electromechanical segregation mechanism. Interestingly all sensor-based ore sorting methods rely on various areas of the electromagnetic spectrum, taking advantage of different materials and object features that respond to the EM waves. The class of sorting lying in the visible spectrum is colour sorting [37], the classification method lying in the infra-red zone is the near infra-red spectroscopy [38], while there are high energy methods such as x-ray spectroscopy and gamma-ray spectroscopy. Despite the application of sensor-based ore sorting, the common objectives are of increased throughput and detection rates. The potential benefits with the use of optical sorters in mineral processing were listed as follows

- Reduction of energy consumption
- Efficient use of mineral resources
- Reduction of water requirements
- Reduction of environmental impact
- Quality increase.

This paper aims to review electromagnetic sensor-based classification criteria used in the sorting system. The focal contributions of this paper are as follows:

1. Provides a comprehensive and up-to-date survey of the electromagnetic spectrum-based classification.
2. Provides comprehensive physics and mathematical modelling embodying each classification.
3. Identifies the different sorting tasks suitable for each band of the spectrum.
4. Identifies the limitation of the sorting method with each EM band.
5. Provides mitigations to tackle weaknesses in each classification scheme.

To the best of our knowledge, this is the first survey paper that provides a comprehensive review of the different EM based sorting methods and proposes a generalized x-ray-based sorting method that addresses most of limitations associated with the different schemes.

The rest of this paper is organized as follows: Section 2 is a deep dive into colour sorting, taking a closer look at reflectance models, and its challenges. Section 3 covers gamma-based sorting and its limitations. In Section 4, is infra-red based sorting and limitations. Section 5 is x-ray-based sorting schemes focusing on transmission and fluorescence as complementary schemes and proposes a new dual x-ray transmission and fluorescence method. Section 6 is a comparative summary of the different EM sorting schemes. Section 7 concludes the paper with a propose future direction.

II. COLOUR BASED SORTING

The intensity of light projected on a sensing pixel gives an object or surface its colour. Discrimination of objects based on their colour is referred to as colour sorting [39]. A color sorting system is dependent on the reflection of light from a surface. An electrical signal proportional to the intensity of reflected light is generated by the transducing circuit. Thus, to evaluate the applicability and effectiveness of a colour-based system to classify materials a brief review of the imaging systems and reflectance models is in order. A colour-based sorting system consists of a lighting source, an object from which the light reflects, a camera system, transducing electronics, a computing system for classification, Fig 1.

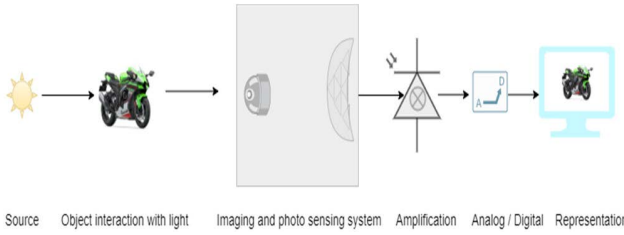

FIGURE 1. Colour classification model system.

The brightness of an object in a scene depends on the reflection of light from it and the way in which the reflection occurs. This brightness is a function of the source, the distance of the object from the source radiance intensity, the angle of incidence of the light source, and the material properties of the object. By considering an infinitesimal surface dA illuminated with a source of flux $d\Phi$ within a solid angle $d\omega$, Fig. 2.

The source radiant intensity, brightness J is given by,

$$J = \frac{d\Phi}{d\omega} \tag{1}$$

Correspondingly the illumination of the element dA, surface irradiance E is given by

$$E = \frac{d\phi}{dA} = \frac{Jd\omega}{dA} \tag{2}$$

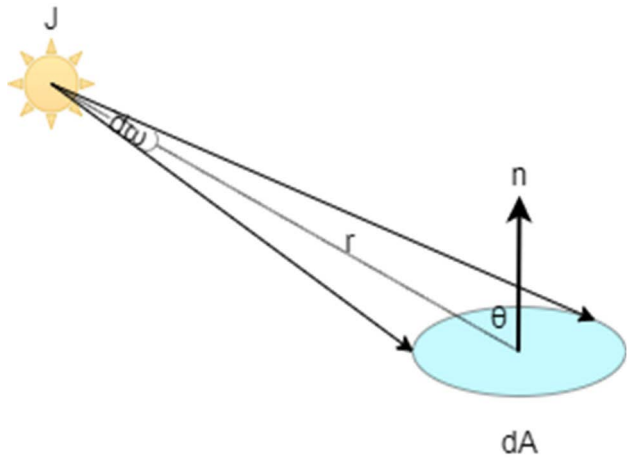

FIGURE 2. Scene brightness model.

While the solid angle $d\omega$ is given by

$$d\omega = \frac{dA cos\theta}{r^2} \tag{3}$$

Such that,

$$E = \frac{J cos\theta}{r^2} \tag{4}$$

Consequently, it is this surface brightness that is reflected towards the sensing device. The brightness of a surface or surface radiance is the flux per unit foreshortened area per solid angle subtended by the receiver, which could be a lens. If the receiver is at an angle θ_r to the normal of the surface under observation, Fig. 2, then the surface radiance L is given by,

$$L = \frac{d^2\phi}{(dA cos\ \theta_r)d\omega} \tag{5}$$

In Fig 3, a camera set up shows how an image is formed on a pixel. The system consists of an infinitesimal element dA_s from which light is cast in the direction of the camera. The light is admitted into the camera through a lens which directs it to a pixel dA_i in the imaging plane. The normal of the surface dA_s makes angle θ with a line of sight, red line. The line of sight makes angle α with the optical axis.

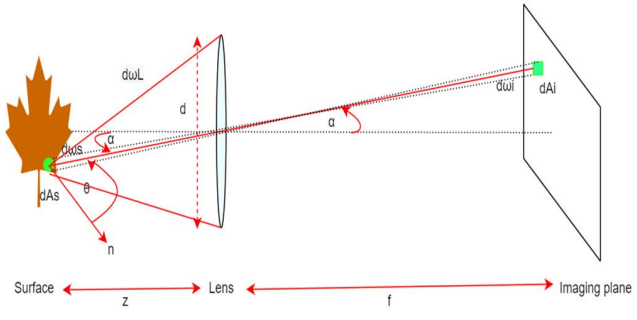

FIGURE 3. Project of an object element onto the imaging plane.

The distance of the element dA_s from to the lens is z, while f is the distance between the lens and the imaging plane. The solid angle subtended by dA_s with respect to the lens is $d\omega_s$ and the solid angle subtended by the imaging pixel dA_i is $d\omega_i$.

From Fig. 3

$$d\omega_s = d\omega_i \tag{6}$$

$$\frac{dA_s \cos\theta}{(z/\cos\alpha)^2} = \frac{dA_i \cos\alpha}{(f/\cos\alpha)^2} \tag{7}$$

$$\frac{dA_s}{dA_i} = \frac{\cos\ \alpha}{\cos\theta}\left(\frac{z}{f}\right)^2 \tag{8}$$

The solid angle subtended by the lens is $d\omega_L$ is

$$d\omega_L = \frac{\pi d^2}{4}\frac{\cos\ \alpha}{(z/\cos\alpha)^2} \tag{9}$$

The light flux received by the lens is equal to the flux received by the pixel. The scene radiance is given by

$$L = \frac{d^2\phi}{(dA_s \cos\ \theta)d\omega_L} \tag{10}$$

and the flux received by the lens is

$$d^2\phi = L(dA_s \cos\theta)d\omega_L \tag{11}$$

The image irradiance E is given by the flux received by the pixel divided by the area of the pixel dA_i.

$$E = \frac{d\phi}{dA_i} \tag{12}$$

Therefore, the flux $d\phi$ received by the pixel

$$d\phi = E dA_i \tag{13}$$

By combining Eqn. 10, 11, and 12,

$$L(dA_s cos\ \theta)d\omega_L = E dA_i \tag{14}$$

And

$$E = L\frac{dA_s}{dA_i} cos\ \theta d\omega_L \tag{15}$$

$$E = L\frac{dA_s}{dA_i} cos\ \theta d\omega_L \tag{16}$$

Using Eqn. 8

$$E = L\frac{cos\ \alpha}{\cos\theta}\left(\frac{z}{f}\right)^2 cos\ \theta d\omega_L \tag{17}$$

And Eqns. 10 - 13

$$E = L\frac{\cos\alpha}{\cos\theta}\left(\frac{z}{f}\right)^2 cos\ \theta\frac{\pi d^2}{4}\frac{cos\ \alpha}{(z/\cos\alpha)^2} \tag{18}$$

Simplifying to

$$E = L\frac{\pi}{4}\left(\frac{d}{f}\right)^2 cos^{\,4}\alpha \tag{19}$$

Giving the relationship between the light cast by the surface L, or scene radiance to the light project on the imaging pixel E. Compactly,

$$E = LC_g cos^4 \alpha \tag{20}$$

where C_g is a property that encapsulates the features of the camera, and can be thought of as camera gain. A key aspect of Eqn. 20 is that the image brightness is independent of scene depth z. Two parameters of interest are L and $\cos^4 \alpha$ term. The $\cos^4 \alpha$ implies that the image brightness falls off quickly as one moves away from the line of sight. The parameter L captures reflectance properties of the material and is associated with the bidirectional reflectance distribution function (BRDF).

A. BIDIRECTIONAL REFLECTANCE DISTRIBUTION FUNCTION

The direction of an incident ray of light in $3D$ space, x, y, z, Fig 4, can be completely defined by its zenith and azimuthal angles $\theta_i \phi_i$ and similarly, the direction of the reflected ray is completely defined by $\theta_r \phi_r$. The ratio of the irradiance due to the source and radiance of an image is called the bidirectional reflectance distribution function [40]. BRDF is a function of $\theta_i \phi_i \theta_r \phi_r$.

$$BRDF = f\left(\theta_i, \phi_i, \theta_r, \phi_r\right) = \frac{L\left(\theta_r, \phi_r\right)}{E\left(\theta_i, \phi_i\right)} \tag{21}$$

This function fully describes the reflectance properties of a surface [41]. In essence, BDRF is a transfer function between the input, scene brightness, and the output, image brightness at the pixel. The reflection of light from a surface is modelled using two types of reflection mechanisms [42]. The first is a specular reflection which is a reflection that occurs at the surface, common with very smooth surfaces, giving surfaces a glossy appearance. The second method of reflection is diffuse reflection, which happens, just below the surface of the material Fig. 5. The interaction of light with the non-homogeneous distribution of sub-surface particles causes the light to refract and be reflected multiple times giving the body a matte appearance [43]. In general, the intensity of a point in the scene is a linear combination of body reflection and surface reflection.

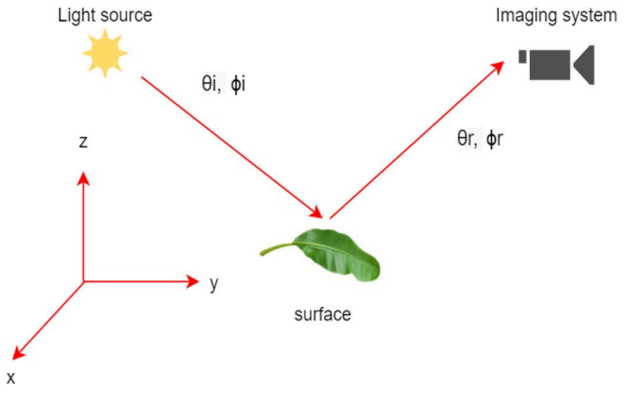

FIGURE 4. Surface radiance model.

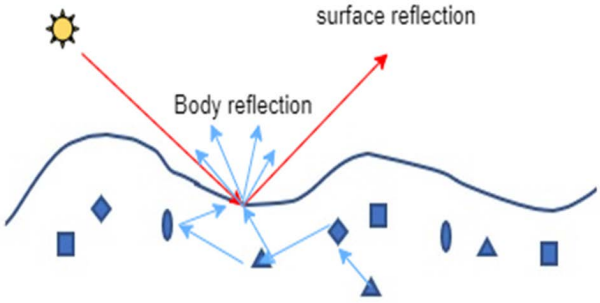

FIGURE 5. Body and surface reflectance.

B. REFLECTANCE MODELS

A commonly used model for body reflection is the Lambertian model that assumes that a surface appears equally bright from all directions [44], namely,

$$f\left(\theta_i, \phi_i, \theta_r, \phi_r\right) = \frac{\rho}{\pi} = constant \tag{22}$$

where ρ is called the albedo of the surface.

$$0 \leq \rho \leq 1 \tag{23}$$

With $\rho = 0$ for perfectly black surface and $\rho = 1$ for the perfectly white surface. In the same macro surface, there exist millions of micro surfaces or infinitesimal surfaces which each has its own albedo, which causes an object to consist of many different intensities or colours. In this case, Eqn. 21 becomes

$$L = E\frac{\rho}{\pi} \tag{24}$$

And from Eqn. 4 for E

$$L = \frac{\rho}{\pi}\frac{J\cos\theta_i}{r^2} \tag{25}$$

But $cos\ \theta_i$ can be expressed vectorially as the projection to normal unit vector $\boldsymbol{n}$ in the direction of the incident ray, such that

$$cos\ \theta_i = \boldsymbol{n} \cdot \boldsymbol{s} \tag{26}$$

And Eqn. 25 becomes

$$L = \frac{\rho}{\pi}\frac{J}{r^2}\boldsymbol{n} \cdot \boldsymbol{s} \tag{27}$$

where $\boldsymbol{s}$ is the unit vector in the direction of the incident light. Thus, for a given incident direction s the surface appears equally bright from all viewing angles. On the other extreme, the second model of reflection is specular of surface reflection in which light is reflected in a single direction. As indicated, the incident light and the reflected light paths can be completely defined by their zenith and azimuth angles. In this case, because there is only one ray of reflected light for each

incident light, the BRDF is defined by a product of two Dirac delta functions,

$$f(\theta_i, \phi_i, \theta_r, \phi_r) = \frac{\delta(\theta_i - \theta_r)\,\delta(\phi_i - \phi_r + \pi)}{\cos\theta_i \sin\theta_i} \tag{28}$$

This means that the camera/observer will see reflection if and only if $\theta_i = \theta_r$ and the azimuthal angles are opposite of each other. The term $cos\ \theta_i\ sin\ \theta_i$ is a term that emanates from the law of conservation of energy.

To account for surface roughness, an infinitesimal surface dA_s, when zoomed consists of micro facets each with their surface normals, but together have an average surface orientation $\boldsymbol{n}$, equal to the normal of the surface $\boldsymbol{dA_s}$ [45]. A good approximation of the distribution of the microsurface normal is given by a Gaussian normal distribution [46],

$$p(\alpha, \sigma) = \frac{1}{\sigma\sqrt{2\pi}} e^{-\frac{\alpha^2}{2\sigma^2}} \tag{29}$$

where σ, is the roughness factor. This leads to the Torrance Sparrow BDRF model [9],

$$f(s, v) = \frac{\rho_s}{(n \cdot s)(n \cdot v)} p(\alpha, \sigma)\, G(n, s, v) \tag{30}$$

where $G(n, s, v)$ is a masking factor related to surface shadowing, namely a surface can be oriented in a way that the reflection from it may be compromised by other facets. A more complete model of a Lambertian model is the Oren-Nayar BRDF model [47]

$$f(\theta_i, \phi_i, \theta_r, \phi_r) = \frac{\rho_d}{\pi}(A + B \cdot \max(0, \cos\phi_i - \phi_r) \sin(\alpha)\tan(\beta)) \tag{31}$$

where A and B are constants dependent on surface roughness and

$$\alpha = max(\theta_i, \theta_r) \tag{32}$$

And

$$\beta = min(\theta_i, \theta_r) \tag{33}$$

As stated earlier, the brightness (colour) of a surface is a function of specular reflection and diffuse reflection,

$$[R_{net} G_{net} B_{net}] = \zeta [R_s G_s B_s] + \eta [R_d G_d B_d] \tag{34}$$

Specular reflection can be a nuisance as it forms highlights that float relative to the light source [48], which can adversely impact on colour sorting in motion-based apparatus.

C. APPLICATION: COLOUR SORTING

Colour sorting is a discrimination technique that is based on the brightness or colour of an object under illumination with a light source. The surface brightness of a surface is a function of the object reflectance properties $f(\theta_i, \phi_i, \theta_r, \phi_r)$ and given a light source and the reflectance properties, the surface radiance can be inferred and used to distinguish material under the same lighting conditions.

Colour-based classification requires a low-cost sensor implementation, however, the mode is sensitive to background light. It is largely dependent on the distinction in colour object or samples to be separated. For example, it can easily be employed in the sorting of ripe and unripe oranges, but in some instances, it may not be adequate to sort ripe oranges from ripe mangos. Where the images of the object are dominated by specular reflection, colour sorting can also be compromised by variation of the surface normal in relation to the imaging system. In the case where samples have a relatively similar colour index, techniques involving boundary features may be adopted to increase the discrepancy, further deep learning methods are now available to manage boundary features that may change based on orientations and other oclusions. Tomra GmBH's Pro Secondary COLOR has been used in the industry to pre-concentrate material from 20 mm to 120 mm particles sizes. The machine consist of high resolution line scan cameras with high color sensitivity. The application range for the Pro Secondary COLOR sorter includes White fillers such as Talc, Calcite, and Marble as well as cement minerals including limestone and gypsum and industrial miinerals of the likes of quartz, magnesite, fluorspar and rock salt. Daria B. Petukhova et al studied principles of color analysis for low contrast mineral using machine vision and developed processing algorithms for color images using samples gold and copper ores and their results confirmed with respect to classification of mineral objects. D. P. Tripathy et al developed a multispectral and joint color texture feature extraction for sorting of limestone ore -gaunge and iron ore/gaunge classification with 98 and 98.4 % recovery rate.

III. GAMMA RAY DETECTION AND SORTING

Gamma-ray detection and sorting is based on the characteristic of some elements to emit gamma rays. Elemental gamma emission is usually a secondary process that follows either beta capture, beta emission, and alpha particle emission [49]. In the case where decay happens because of alpha particle decay, an atomic species of atomic number Z and mass number A, the following process entails alpha particle decay

$${}^{A}_{Z}P \rightarrow {}^{4}_{2}He + {}^{A-4}_{Z-2}D^{*}. \tag{35}$$

In most cases the new species ${}^{A-4}_{Z-2}D^{*}$ exist in an excited state and is stabilized by the emission of a gamma photon.

$${}^{A-4}_{Z-2}D^{*} \rightarrow {}^{A-4}_{Z-3}D + {}^{0}_{0}\gamma + {}^{0}_{1}\bar{\nu} \tag{36}$$

Another mode of gamma-ray emission follows a beta decay process.

$${}^{A}_{Z}P \rightarrow {}^{0}_{0}\beta^{-} + {}^{A}_{z+1}Q^{*} + {}^{0}_{1}\bar{\nu} \tag{37}$$

$${}^{A}_{z-1}Q^{*} \rightarrow {}^{A}_{z-1}Q + {}^{0}_{0}\gamma \tag{38}$$

Beta and alpha particles have weak penetration power [12], Fig. 6, thus while they are subjects of the radiative process, they do not play an important role in gamma-ray detection.

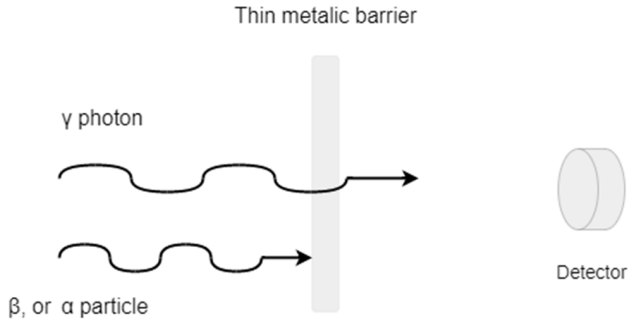

FIGURE 6. Alpha, beta, and gamma-ray penetration.

The rate of emission of gamma-ray emission is proportional and characterized by the material decay equation

$$R = \frac{dN}{dt} = -\lambda N = -\lambda N_o e^{-\lambda t} \tag{39}$$

where N is the number of radioactive atomic species, and λ is the decay rate which is a unique material feature that can be used to classify different materials. In sorting applications, the measurement involving gamma radiation is done within a very short period such that the rate of nucleic disintegration can be accurately approximated by:

$$R = \frac{dN}{dt} - \lambda N_o \tag{40}$$

where N_o is the number of radiative atomic species presented to the sensing zone. The subsequent gamma emission by a daughter nucleus has an associated lifetime that plays an important role in the application feasibility and or machine productivity [50]. Additionally, another intrinsic property of the radiation is a unique energy distribution function also characteristic to the sample under observation. Enough time must be allowed for the process to occur to obtain a good signal for detection. In gamma-ray sorting, the task of sorting starts with determining the count rate of the emitted gamma rays.

A. APPLICATION OF GAMMA-RAY DETECTION IN SORTING

Sorting using gamma-ray detection is a surrogate sorting method as in most cases the element or material being sorted for is not primarily radioactive, however, is usually found to be associated with a radioactive element. For example, in the sorting of gold, there are some gold ores which is associated with uranium, and the task sorting for gold simply becomes detecting and classifying through gamma-ray activity [51]. Eqn. 39 indicates the dependence of the activity of the number of atomic species present in the ore particle. For a given ore particle size or mass, the total mass of the sample is the sum of the mass of the gold-bearing portion and the mass of uranium such that,

$$m_{op} = m_{au} + m_u \tag{41}$$

where m_{op} is the total mass of the ore particle presented to a sorting station and m_{au} and m_u are the mass of gold *(Au)* and uranium (U) respectively. For pure uranium sorting Eqn. 39 provides a simple method of sorting because by conditioning material entering the sorter through screening the input material to a given particle size, R is completely determined because both λ and N_o will be knowns of Eqn. 39. However, in surrogate sorting an interesting dynamic is introduced by Eqn. 41 in which the size or mass of each constituent cannot be predetermined. The constituents are associated with each other through a joint Gaussian distribution but with a strict condition against mutual exclusivity, namely,

$$P(m_{au} \cap m_u) \neq 0 \tag{42}$$

This condition guarantees that whenever uranium is detected, it shall be found with some gold. This prior knowledge of the problem, the inherent natural ore correlation between gold and uranium, provides for a simple gamma-ray detection sorting method to be adopted.

B. APPROACHES TO SORTING

Colour Fig. 7 shows a schematic of a sorting system consisting of a conveying system carrying material towards the sensing zone. A gamma detector is placed in the trajectory of the particles and records counts of gamma rays in each of the particles. Upon detection of a given threshold level, the controller sends an activation to the pneumatic solenoid valve to eject the desired particle to accept the bin.

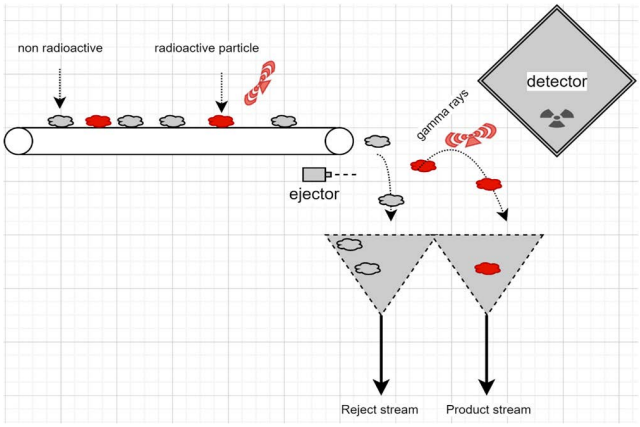

FIGURE 7. Gamma-ray sorter.

C. DETECTIO

Fig. 8 shows a lumped element model of a counting detector operated in pulse mode. The output voltage $V(t)$ from a single radiation event is influenced by the response of the

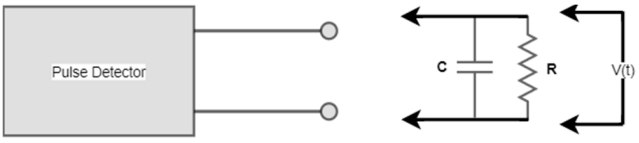

FIGURE 8. Pulse detector equivalent circuit.

circuit to which the detector is connected. This signal is pre-amplified before final measurement. R and C represent the equivalent resistance and capacitance of the measuring instrument and the detector. An important case for optimal operation in pulse mode is when the time constant of the circuit is much larger than the charge collection time to allow for the detector to collect the necessary charge before a current can flow in the resistor R [52]. This also ensures that the detector circuit is completely decoupled from the external circuit. The amplitude of the output voltage signal is equal to the ratio of the total charge created per incident photon and the circuit capacitance C, which is a fixed parameter. Thus

$$V_{max} = \frac{Q}{C} \tag{43}$$

Consequently, the output of a detector in pulse mode is a series of discrete pulses, each with a Q proportional to the energy of the incident gamma photon [53]. The amount of charges transported and transferred into the detector is a Gaussian random variable [54], this distribution is unique to the radioactive nuclide, and measurement of the amplitude distribution can be used to infer about the incident gamma events [55]. The determination of low threshold limits for detection is guided by the levels of background radiation present in the application. A common way of representing pulse height distribution is through the differential pulse amplitude distribution. Fig. 9 is a typical pulse amplitude. Where E is the energy carried by each gamma radiation and dN/dE is the number of gamma radiation with an energy range E an $dE + dE$. By integrating the interactions over a long enough period, the result is the number N_γ of gamma photons arriving at the detector with a given time period, dT. The number constant $\frac{N_\gamma}{dT}$ is proportional to sample activity rate R in Eqn. 61.

$$N_\gamma = \int_0^\infty \frac{dN}{dE} dE \tag{44}$$

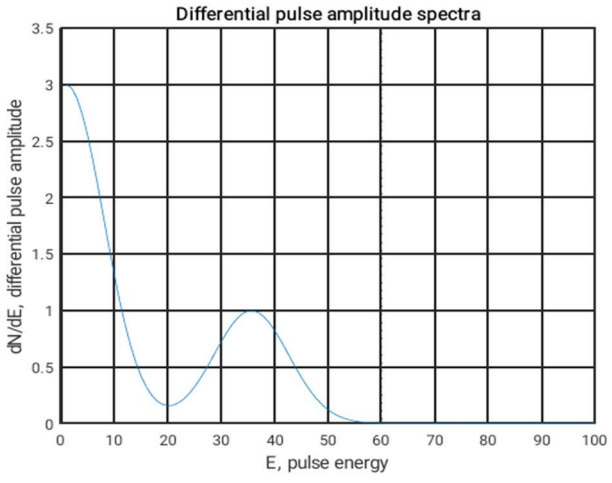

FIGURE 9. Differential pulse amplitude spectra.

As stated, applications of gamma-ray sorting typically involve the desired mineral which is always attached to some radioactive substance, such as gold and uranium and some waste non-radioactive substance. This simplifies the sorting principle as the objective becomes only to detect radiation greater than the threshold background. This settles the challenge cause the randomness in the size of N_o or equivalently mu.

D. DETECTOR ENERGY RESOLUTION

The response of a detector to a monochromatic beam of photons determines its resolution [56]. Ideally, a detector with spectral response equivalent to distribution approximating a Dirac delta function is defined as high resolution [57]. In such cases, the variance between measurements of the same energies is close to zero. Fig. 10 are spectral responses of two detectors overlayed on each other.

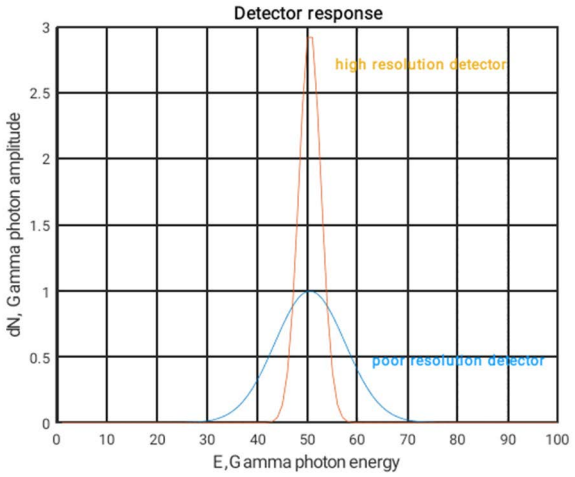

FIGURE 10. High-resolution detector response and low-resolution detector response.

While detector resolution may be important where sorting involves more than one radioactive source, it is not the case in most applications as only one primary element has activity. As this method relies only on the detection of present radiation, detector response spectra do not play a significant distinguishing factor. A measure of detector resolution is defined as the ratio of the full width half maximum spread divided by the average detector response energy and is given by

$$D_r|_{poisson\ limit} = \frac{FWHM}{E_o} = 2.35\sqrt{\frac{F}{N}} \tag{45}$$

where F is the Fano Factor, which is significantly lower than unity for semiconductor diode detectors and close to unity for scintillation detectors. Cleary Detectors with a Fano factor much less than unity are classified to have better resolution than those with a Fano factor approaching unity. Additionally, the resolution is a function of the number of incident gamma

radiation events arriving at the detector, and the more events the better resolution.

E. DETECTION EFFICIENCY

Gamma radiation is uncharged radiation, and it can travel significant distances in the detector active area before exciting enough ion pairs along its path for ease of recording [58]. As gamma rays have a large mean free path in the detector, they are not 100 % efficient. Two measures of efficiency are used together to describe detector efficiency, there are absolute efficiency and intrinsic efficiency. Absolute efficiency is defined as

$$\epsilon_{abs} = \frac{number\ of\ pulses\ recorded}{number\ of\ radiation\ quanta\ emitted\ by\ source} \tag{46}$$

While intrinsic efficiency is defined as

$$\epsilon_{int} = \frac{number\ of\ pulses\ recorded}{number\ of\ radiation\ quanta\ incident\ on\ the\ detector} \tag{47}$$

Absolute efficiency is a function of detector material properties and counting geometry [59], while intrinsic efficiency on the other hand does not account for the solid angle subtended by the detector and depends primarily on detector material, quanta energy, and dimensions of the detector in the direction of the incident radiation. For isotropic detectors, the two efficiencies are related by

$$\frac{\epsilon_{int}}{\epsilon_{abs}} = \frac{4\pi}{\Omega} \tag{48}$$

where Ω is the solid angle of the detector with respect to the source position. For a detector with right circular geometry as in Fig. 11, the solid angle Ω is given by

$$\Omega = 2\pi\left(1 - \frac{d}{\sqrt{a^2 + d^2}}\right) \tag{49}$$

$$Ford \gg a,$$

$$\Omega = \frac{\pi a^2}{d^2} \tag{50}$$

$$\frac{\epsilon_{abs}}{\epsilon_{int}} = \frac{\Omega}{4\pi} = \frac{a^2}{4d^2} = 0.25r^2 \tag{51}$$

where $r = a/d$,

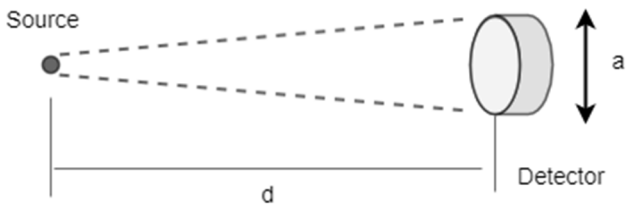

FIGURE 11. Solid angle for a detector with circular geometry.

Which says efficiency is a function of the area coupling the radiation and inversely proportional to the square distance between source and detector. A more complex geometrical

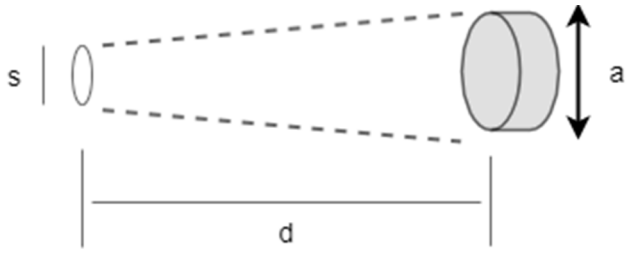

FIGURE 12. Uniform circular source and circular detector.

detector setup includes a uniform circular source aligned with a circular detector as in Fig. 12. The effective solid angle subtended in this arrangement is given by

$$\Omega = \frac{4\pi a}{s}\int_0^\infty \frac{exp\,(-dk)\,J_1\,(sk)\,J_1(ak)}{k}dk \tag{52}$$

where $J_1\,(x)$ are Bessel function of the first kind. Ω can be viewed as a Fourier transform to the two Bessel functions.

A three-term approximation of Eqn. 69 is

$$\Omega \cong 2\pi\left(1 - \frac{1}{(1+\beta)^{\frac{1}{2}}} - \frac{3}{8}\frac{\alpha\beta}{(1+\beta)^{\frac{5}{2}}}\right) \tag{53}$$

where $\alpha = \left(\frac{a}{d}\right)^2$ and $\beta = \left(\frac{s}{d}\right)^2$. This approximation becomes inaccurate when the detector or source dimensions are too large relative to the spacing.

F. DEAD TIME EFFECTS

In a pure counting system, it is imperative to be able to distinctly measure the interaction of each gamma photon with the detector. As radioactive decay is a random process, at times, it is impossible to accurately count all events of interaction. The minimum time separating two events is called dead time. At times detector aliasing is influenced by the electronics coupled to the detector circuit. However, in gamma radiation detection in which there is only one active source present, dead time does not pose a problem, as the criteria are focused on detecting the presence of gamma photons and not spectrographic information.

G. GAMMA SPECTROSCOPY APPLICATION SCOPE

Gamma-based classification methods are limited to a case where a sample consists of non-radioactive and radioactive components. Further, since the differential pulse amplitude spectra are unique for each radioactive substance, the method of spectroscopy enables the separation of samples based on their unique spectra. Since gamma is a secondary process, the speed of counting is influenced by dead time zones and the time to integrate the differential pulse height spectrum.

IV. INFRA-RED SPECTROSCOPY

Characterization based on infra-red spectroscopy stems from the idea that some molecules can absorb infra-red radiation [60]. Each molecule that absorbs infra-red can only absorb a unique portion of the infra red spectrum leading to

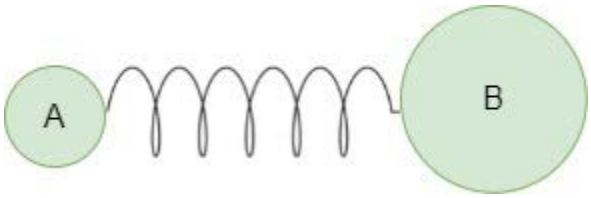

FIGURE 13. Hooke's law representation of molecular atomic vibrations.

an IR fingerprint [60]. A molecule or functional group can be identified by comparing its spectrum with the spectra of known samples. The determinant of which energy band of the infra-red to be absorbed is the bond strength and mass of the entire molecular structure [61]. Fig. 13 shows a type of bond, a single covalent bond from the joining two conceptual atoms A and B, with mass m_a and m_b. The force of attraction that holds the molecule together determines the bond strength, natural vibration frequency, and the band of an infra-red band which can be absorbed by the molecule. The force of attraction between the molecules is defined by Hooke's law

$$F = -kx \tag{54}$$

where k is force constant, related to the bond strength and x is the bond length displacement from equilibrium. In the absence of any external force or exciter, application of Newton second law, the sum of forces on the body is equal to zero, namely

$$\mu \frac{d^2x}{dt^2} + kx = 0 \tag{55}$$

Or

$$x'' + \frac{k}{\mu}x = 0 \tag{56}$$

with a homogeneous solution,

$$x\,(t) = Acos(\nu t) \tag{57}$$

where

$$\nu = \sqrt{\frac{k}{\mu}} \tag{58}$$

where μ is the reduced mass of the system, and for a two-constellation system

$$\mu = \left[\sum\nolimits_{i=1}^{N} \frac{1}{m_i}\right]^{-1} \tag{59}$$

A prerequisite for infra-red absorption for a molecule to have a non-zero dipole moment as it vibrates or rotates. A dipole moment results from the difference in electronegativity of the participating atoms in the molecule covalent bond or in the ionic bond. The magnitude of the dipole moment is a function of net electronegativity and the bond length. When the net electronegativity is non-zero molecular is vibrations or rotations cause a field that interacts with IR radiation. The geometry of the molecule plays a significant part in the resultant dipole moment. This condition precludes detecting symmetric molecules by means of infra-red spectroscopy.

Table 1 shows the influence of net electronegativity and molecular geometry on the resultant molecular dipole moment. Part *b* is the *trans*-isomer of dichloromethane or methylene chloride while part *a* is the *cis*-isomer of the same molecule. The pairwise diatomic polarization is shown with an orange vector pointing toward the atom possessing higher electronegativity. By inspection of the vector sum of the *cis* isomer, the dipole moment is non-zero, while the *trans* isomer has zero net dipole moment.

Subscript on the δ is the element symbol

The 1-D harmonic potential associated with a displacement x from equilibrium is

$$V(x) = \frac{1}{2}kx^2 \tag{60}$$

The corresponding 1-D Schrodinger equation is

$$-\frac{\hbar}{2\pi}\frac{d^2\Psi}{dx^2} + V\,(x)\,\Psi\,(x) = E\Psi\,(x) \tag{61}$$

Whose solutions energy levels are

$$E_v = \left(v + \frac{1}{2}\right) h\nu_e, \text{for } v = 1, 2, 3, \ldots, \infty \tag{62}$$

$$\nu_e = \frac{1}{2\pi}\sqrt{\frac{k}{\mu}} \tag{63}$$

When a more general approach is considered, factors such as anharmonicity of the potential play a significant role in the form of E_v and when centrifugal stretching, vibrational and rotational interactions are included [62],

$$E_v = \left(v + \frac{1}{2}\right) h\nu_e - \left(v + \frac{1}{2}\right)^2 X_e h\nu_e + B_e J\,(J+1) - D_e J^2\,(J+1)^2 - \alpha_e \left(v + \frac{1}{2}\right) J(J+1) \tag{64}$$

where the second term represents anharmonicity, the third is Coriolis coupling, forth centrifugal stretching, while the firth term represents rovibrational coupling.

When a source of continuum infra-red energy is applied to the molecule, the vibrational modes can be promoted to a higher quantum state by absorption of photons with a specific energy equivalent to the molecular vibrational mode. The difference in energy absorbed is equal to the energy of the infra-red photon energy of a distinct frequency. A simplistic arrangement of source, sample, and detector in absorption and a typical IR spectrum expected is as in Fig. 14.

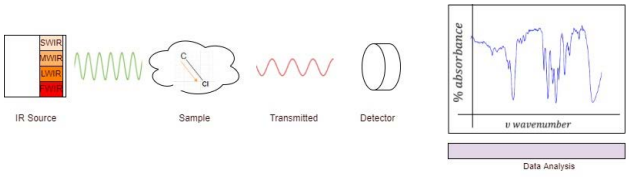

FIGURE 14. Simplistic arrangement of source, sample detector in IR measurements.

TABLE 1. Cis and trans-isomers of dichloromethane, atomic electronegativity, and diatomic polarization.

Isomer	Molecular geometry	Atomic electronegativity	Diatomic polarization
(a) Cis	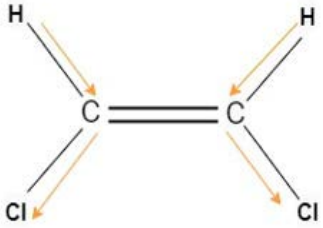	$\delta_h^- = 2.2$	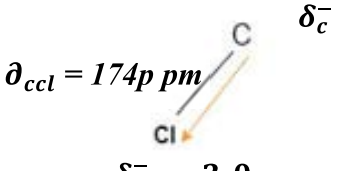
		$\delta_c^- = 2.55$	$\delta_{cl}^- = 3.0$
(b) Trans	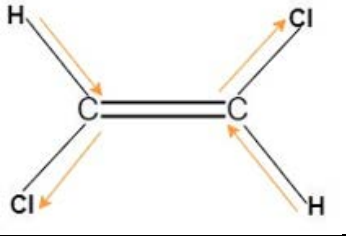	$\delta_{cl}^- = 3.0$	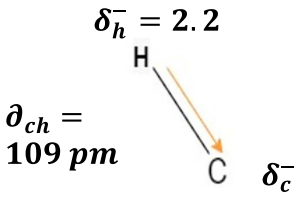

The relationship between the intensity of infra-red radiation received at the detector is proportional to the square change in dipole moment with respect to vibrational coordinate, namely

$$I_{IR} \propto \left(\frac{d\tau}{dx}\right)^2 \tag{65}$$

where τ is the dipole moment, x vibrational coordinate, and$q$ is the net electronegativity charge

$$\tau = qx \tag{66}$$

A. INFRA-RED SPECTROSCOPY APPLICATION SCOPE

IR spectroscopy can obtain information from a whole range of frequencies simultaneously within orders of a second. When applied in Fourier Transform spectrometer, IR resolution can be as low as 0.1 – 0.005 cm^{-1} [63], also in this mode, the IR spectrometer doesn't require the use of a slit and a monochromator. It has a wide range of applications from organic materials to some inorganic materials. However, this method is limited to a class of samples whose molecular polarity is none zero, limiting its scope of application and being unable to detect certain isomers of the same element.

V. X-RAY BASED SORTING

X-rays are electromagnetic waves with energies ranging from 500 eV to 500 keV or (25 A – 0.25 A). EM waves in this band are absorbed by matter through photoelectric effect [64]. Electrons at the core level, i.e., 1s and 2p orbital shells, are tightly held within stable atomic orbitals by the force of the nucleus [65]. When x-rays are incident on an atom, the electrons in the inner shell orbitals gain energy, and depending on the magnitude of incident energy, the electrons can either be promoted to high energy shells, or if the energy is sufficient electrons can be lost to the continuum. However, if the incident x-rays do not possess energy greater than the binding energy of the core level electrons, such x-rays will not be absorbed [66]. Conversely, it is possible for x-rays will sufficiently greater energy than the core electrons to cause the core electrons to be ejected to a continuum, in which the x-rays will be destroyed through total absorption. The energy transferred to such electrons will be equal to the electron binding energy and kinetic energy of the ejected photoelectron. When the incident x-rays have equal or greater energy than the binding energy of the core electron the absorption process gives rise to X-ray absorption fine structure (XAFS) phenomena [67].

X-ray absorption fine structure (XAFS) spectra can be determined for all elements in the periodic table [68]. The beauty of the XAFS technique is that it is not phase-dependent or does not require homogeneity or crystallinity [69]. X-rays are penetrative and measurements are not influenced by surface conditions [70]. XAFS measurements can be done for extreme conditions including high temperature and pressure and can be done for elements that appear in trace proportions within a sample [71].

Atoms generally desire to maintain a stable electron configuration by absorbing an electron from the outer shells. Since outer orbitals possess higher energy levels than inner shells, a transition from the higher energy state to lower energy is associated with emission radiation. The energy released in this transition is proportional to the discrete quantum states and wavelength. Additionally, the incident energy can be scattered by the nucleus potential causing the energy of the incident x-rays to be absorbed by the target atom. Different atoms, an consequentl, materials absorb and scatter incident x-rays uniquely based on the characteristics of the atoms constituting that material [72]. This characteristic

information has been used widely in identification or classification.

The probability that x-rays will be absorbed in the matter is given by Beer–Lambert's law

$$I = I_0 exp(-\mu t) \tag{67}$$

where I_0 is the intensity of incident x-rays, I is the intensity of x-rays transmitted through a sample of thickness t, and μ is the absorption coefficient which is a material characteristic. Written in logarithmic form Eqn. 67, is an EMF equivalent of ohms, causing μ to analogous to the common electrical resistance, i.e.

$$\log I = \log I_0 - \mu t \tag{68}$$

$-\mu t$ is the intensity drop across the material. For a given element, x-rays can be tuned to an energy level equal to the core electron binding energy. In this condition a sharp rise or absorption edge in absorption spectra is observed, indicating promotion of the core electron to a continuum. Different characteristic spectral lines are observed depending on the atom and on transition states, for example, a $k\alpha_1$, $k\beta_1 L\alpha_2$ represents a transition from $1s$ to $2p$, $1s$ to $3p$, and $2p$ to $3d$ respectively.

X-ray fluorescence and the Auger effect are the two main mechanics of decay for an excited state. In fluorescence, a higher energy core-shell / orbital electron drops to complete the core hole created through absorption, ejecting x-rays with energy equivalent to the change in quantum states. The influencing factor driving the decay is the interaction of the core electrons with the potential of the nucleus. This interactive influence carries information about the nucleus and hence the type and concentration of a given atomic species in the sample. For elements other than the hydrogen atom, the change in energy because of a drop from n_1 to n_2 is given by Moresly's law,

$$\Delta E_{n_{1,2}} = -13.6\left(\frac{1}{n_2} - \frac{1}{n_2}\right) Z_{eff}^2 \tag{69}$$

where Z_{eff}, the effective nuclear charge, which accounts for the nucleic charge Z and the shielding electrons S.

$$Z_{eff} = Z - S \tag{70}$$

Since each element has a unique Z_{eff}, the spectral lines of each element would be different. While the variation Z_{eff} for two consecutive elements is equal to 1, that of Z_{eff}^2 is significant for proper distinction in spectral lines. For example, for two elements with atomic number Z and $Z+1$, the variation in Z_{eff} is

$$\Delta Z_{eff}^2 = 2Z - 2S + 1 \tag{71}$$

If $Z \gg 1$ and S is in the order of $0.1Z$, the measure of ΔZ_{eff}^2 separation relative to Z is 180 % for two consecutive elements, while the measure of separation of Z_{eff} relative to Z for any $Z > 10$ is less than 10 %.

In Auger de-excitation, an electron relegates from higher energy together with a second electron being ejected to a continuum. The path of whether a de-excitation goes through fluorescence or Auger effect depends on Z and the energy level but the probability of emission is directly proportional to absorption probability.

A. X-RAY MEASUREMENT MODE

1) FLUORESCENCE / LUMINESCENCE MODE

Measurement in x-ray fluorescence is an investigation of secondary emitted x-rays because of transitions between higher core electron and a core hole, or visible light (Luminescence) emitted by a sample as part of myriad de-excitation events [73]. The intensity of fluoresced x-rays is a function of the absorption coefficient is given by

$$I_f = \frac{I_o \epsilon \Delta\Omega}{4\pi} \frac{\mu_x(E)\left(1 - exp\left(-\left(\frac{\mu_T(E)}{sin\ \theta} + \frac{\mu_T(E_f)}{sin\ \phi}\right)t\right)\right)}{\frac{\mu_T(E)}{\sin\ \theta} + \frac{\mu_T(E_f)}{\sin\ \phi}} \tag{72}$$

where I_o is the source x-ray intensity, ϵ is the fluorescence efficiency, $\Delta\Omega$ is the solid angle, E_f is the fluoresced x-ray energy, θ is the angle between the normal of the sample and the source, ϕ is the exit angle of the fluoresced x-ray, $\mu_x(E)$ is the absorption coefficient of the element of interest, $\mu_T(E)$ is the total absorption in the sample and t is the escape depth of the fluoresced x-rays.

$$\mu_T(E) = \mu_t(E) + \mu_o(E) \tag{73}$$

where $\mu_t(E)$ and $\mu_o(E)$ are the absorption coefficients of the target material and other material respectively. Fig. 15 is a configuration for an x-ray machine in fluorescence /luminescence measurement mode

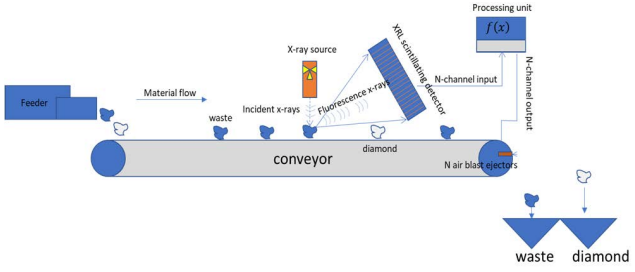

FIGURE 15. X-RAY fluorescence machine cross-section.

Measurement in fluorescence mode is affected by sample dimensions and concentration. For thin dilute sample $\mu_t(E) \ll \mu_o(E)$ and

$$\left(\frac{\mu_T(E)}{sin\ \theta} + \frac{\mu_T(E_f)}{sin\ \phi}\right) t \ll 1 \tag{74}$$

such that

$$exp\left(-\left(\frac{\mu_T(E)}{sin\ \theta} + \frac{\mu_T(E_f)}{sin\ \phi}\right)t\right) \cong 1 - \left(\frac{\mu_T(E)}{sin\ \theta} + \frac{\mu_T(E_f)}{sin\ \phi}\right)t. \tag{75}$$

reducing Eqn. 72 to

$$I_f = \frac{I_o \epsilon \Delta\Omega}{4\pi} \mu_x(E) t \tag{76}$$

making the fluoresced intensity be a function of the fluorescent efficiency ϵ, detector solid angle $\Delta\Omega$, absorption coefficient $\mu_x(E)$ and thickness. For thick dilute sample, namely $\mu_t(E) \ll \mu_o(E)$ and

$$\left(\frac{\mu_T(E)}{sin\,\theta} + \frac{\mu_T(E_f)}{sin\,\phi}\right) t \gg 1 \tag{77}$$

Eqn. 10 reduces to

$$I_f = \frac{I_o \epsilon \Delta\Omega}{4\pi} \frac{\mu_x(E)}{\frac{\mu_T(E)}{sin\,\theta} + \frac{\mu_T(E_f)}{sin\,\phi}} \tag{78}$$

In this case $\mu_T(E)$ can also be ignored, further reducing the measurement problem to

$$I_f \propto I_o \mu_x(E) \tag{79}$$

In mineral processing, the problem of classification is a lot easy since the minerals μ_x and gangue materials $\mu_o(E)$ are presented to the sorting station in their discrete pure form. Thus, for each particle presented to the x-rays, for pure mineral of interest $\mu_o(E) = 0$ and for pure gangue materials $\mu_t(E) = 0$. Where a particle consists of both the target material and gangue material, a further comminution process may be desired to liberate the mineral for gangue. There are cases where the proportion is relatively comparable, in such a case further comminution may be detrimental to the target material, especially in cases where breaking the target material results in loss of value.

Strictly speaking, a pure thin sample is equivalent to a thick dilute sample as long as for such samples.

$$exp\left(-\left(\frac{\mu_T(E)}{sin\,\theta} + \frac{\mu_T(E_f)}{sin\,\phi}\right) t\right) \cong 1 - \left(\frac{\mu_T(E)}{sin\,\theta} + \frac{\mu_T(E_f)}{sin\,\phi}\right) t \tag{80}$$

An interesting fact is that a pure thin sample represents a much thicker sample than a thick dilute sample as

$$\mu_t(E) < \mu_t(E) + \mu_o(E) \tag{81}$$

which is a good consequence for mineral processing/ for classification between samples that occur in their purest form. This also helps in aligning the calibration process for detection to the element of interest only.

2) FLUORESCENCE SELF-ABSORPTION

Fluorescence measurements are susceptible to self-absorption for thick samples and also for high energy application [38]. The thick sample fluorescence model eqn. 72, has a self absorption component described as

$$f(E) = \frac{\mu_x(E)}{\frac{\mu_T(E)}{sin\,\theta} + \frac{\mu_T(E_f)}{sin\,\phi}} = \frac{\mu_x(E)}{k_\theta \mu_T(E) + k_\phi \mu_T(E_f)} \tag{82}$$

where $k_\theta = 1/\sin\theta$ and $k_\phi = 1/\sin\phi$

We can write $\mu_T(E)$ as

$$\mu_T(E) = c_x \mu_x + \sum_{i=2}^{N} c_i \mu_i \tag{83}$$

where μ_x is the absorption coefficient of the target material, and the indices $i = 2..N$, are for absorption coefficients of other materials found the sample. Therefore, eqn 82 becomes

$$f(E) = \frac{\mu_x(E)}{k_\theta \left(c_x \mu_x + \sum_{i=2}^{N} c_i \mu_i\right) + k_\phi \mu_T(E_f)} \tag{84}$$

To minimize self-absorption, $f(E)$ must be maximized

$$\frac{df}{dE} = 0 \tag{85}$$

Therefore, equation (86), as shown at the bottom of the page.

Cleaning it up and re-arranging

$$\frac{d\mu_x}{dE} = \frac{\mu_x k_\theta \sum_{i=2}^{N} c_i \frac{d\mu_i}{dE}}{k_\theta \sum_{i=2}^{N} c_i \mu_i + k_\phi \mu_T(E_f)} \tag{87}$$

$$\int \frac{d\mu_x}{\mu_x} = \int \frac{k_\theta \sum_{i=2}^{N} c_i \frac{d\mu_i}{dE}}{k_\theta \sum_{i=2}^{N} c_i \mu_i + k_\phi \mu_T(E_f)} dE \tag{88}$$

Both LHS and RHS of eqn 88 are of the form

$$\int \frac{\dot{f(x)}}{f(x)} dx \tag{89}$$

So that $f(E)$ is maximized for

$$\mu_x(E) = k_\theta \sum_{i=2}^{N} c_i \mu_i(E) + k_\phi \mu_T(E_f) \tag{90}$$

This is an interesting result which in some way is a statement of conservation of energy.

Substituting eqn. 90 into $f(E)$

$$f(E) = \frac{\mu_x(E)}{k_\theta \left(c_x \mu_x + \sum_{i=2}^{N} c_i \mu_i\right) + k_\phi \mu_T(E_f)}$$

$$f(E) = \frac{\mu_x}{k_\theta c_x \mu_x + \left[\sum_{i=2}^{N} c_i \mu_i + k_\phi \mu_T(E_f)\right]} \tag{91}$$

$$\frac{df}{dE} = \frac{\left(\left[k_\theta \left(c_x \mu_x + \sum_{i=2}^{N} c_i \mu_i\right) + k_\phi \mu_T(E_f)\right]\right) \frac{d\mu_x}{dE} - \mu_x \left(k_\theta c_x \frac{d\mu_x}{dE} + k_\theta \sum_{i=2}^{N} c_i \frac{d\mu_i}{dE}\right)}{\left[\mu_x \left(c_x \mu_x + \sum_{i=2}^{N} c_i \mu_i\right) + k_\phi \mu_T(E_f)\right]^2} = 0$$

$$\times \left(\left[k_\theta \left(c_x \mu_x + \sum_{i=2}^{N} c_i \mu_i\right) + k_\phi \mu_T(E_f)\right]\right) \frac{d\mu_x}{dE} - \mu_x \left(k_\theta c_x \frac{d\mu_x}{dE} + k_\theta \sum_{i=2}^{N} c_i \frac{d\mu_i}{dE}\right) = 0 \tag{86}$$

From eqn. 90 the term in the square parentheses equal μ_x, such that the maximum

$$f(E) = \frac{1}{k_\theta c_x + 1} \tag{92}$$

Or

$$f(E) = \frac{\sin\theta}{c_x + \sin\theta} \tag{93}$$

Since θ is independent of energy, we can further differentiate f with respect to θ to obtain the best angle of incidence that helps in mitigating self-absorption, and this gives $\theta = \pi/2$. So that the best value of $f(E)$ is

$$\frac{1}{c_x + 1} \tag{94}$$

Hence by equating eqn 82 and 94 and solving for E, gives the best x-ray operating energy for given system consisting of concentrations c_x of the target material.

Noting that the denominator of $f(E)$ is a function of energy, to anihilate the energy dependence, ϕ is adjusted such that

$$1/\sin\theta \ll 1/\sin\phi \tag{95}$$

This makes the term containing k_ϕ in eqn 82 more dominant such that ignoring the first term of the denominator admissible, leading to

$$I_f = \frac{I_o \epsilon \Delta\Omega}{4\pi k_{f\phi}} \mu_x(E) \tag{96}$$

where $k_{f\phi} = \frac{\mu_T(E_f)}{sin\phi}$

With the above steps, we have,

- Obtained the best angle of incidents that minimizes self-absorption.
- Can obtain the best x-ray operating energy to minimize self-absorption

In transmission mode, our biggest challenge is inter-particle contrast, particularly for thin samples. For example, for two materials with absorption coefficient μ_1 and $\mu_2$respectively, a ratio based inter-particle contrast, C_{T12} is I_{m1}/I_{m2},

$$C_{T12} = e^{-(\mu_1 - \mu_2)t} \approx 1 - (\mu_1 - \mu_2)\, t \approx 1 \tag{97}$$

$$\text{for } (\mu_1 - \mu_2)\, t \ll 1 \tag{98}$$

This implies that the detector will not be able to distinguish between materials because a result of unity implies the materials are the same. The thin fluorescent sample case is as defined by eqn. 99. Interestingly the inter-particle contrast for fluorescence measurement is the same for both thin and thick samples and is given by

$$C_{f12} = \frac{\mu_1}{\mu_2} \tag{99}$$

In the large sample case of transmission, interparticle contrast is defined as

$$C_{T12} = e^{(\mu_2 - \mu_1)t} \tag{100}$$

which tends to 'infinity' as the product $(\mu_1 - \mu_2)\, t \gg 1$ for a large sample case, which a good feature for classification.

3) TRANSMISSION MOD

The basis of x-ray in transmission mode is the Beer-Lambert absorption eqn. 101.

$$I = I_0 exp\,(-\mu_T(E)t) \tag{101}$$

where, $\mu_T(E)$ is the sample absorption coefficient, t is the sample thickness and I_o, I_t are the incident x-ray and transmitted x-ray intensities respectively. The technique exploits the fact that different elements or atoms absorb radiation differently due to the difference in atomic density. The absorption coefficient is a well-behaved function of energy [40] which is dependent on sample density, atomic number Z, atomic mass A, and x-ray energy E roughly as given by the Eqn. 17 as:

$$\mu(E) \approx \frac{\rho Z^4}{AE^3} \tag{102}$$

The Z^4 dependence leads to well-separated μ values at a given operation energy E. This is a useful property in various x-ray imaging classification methods including sorting, medical imaging, and computed tomography [74]. A general rule of thumb for consideration of measurement in transmission mode for when the element of interest is significant in the entire sample, typically $\mu_x(E) > 10\%\mu_T(E)$. However, to obtain enough absorption, the product of the thickness of the sample together with its aggregated absorption coefficient must be at least 2.5 above the absorption edge [42], namely,

$$\mu_T(E)\, t - absorption\ Edge > 2.5 \tag{103}$$

else the signal through the sample may not be able to transfer the atomic information to the detector or imaging system. In a sorting application, which is different from elemental composition analysis, samples presented to the measurement system are either pure or gangue. This makes the sorting tasks a lot easier than elemental analysis.

It is useful to determine $\mu_T(E)$ by means of current meaurements at the detector. More detail about the element under observation can be obtained when the absorption coefficient is considered in its extende x-ray absorption fine structure model, which is describe by Eqn. 104 [75].

$$\mu(E) = \mu_0(E)\,(1 + \chi(E)) \tag{104}$$

Transforming from energy space into the wavenumber space, leads to

$$\chi(E) :\rightarrow \chi(k) = \sum_{i=1}^{N} \frac{N_i f_i(k)\, exp(-2k^2\sigma_i^2)}{kR_i} sin\,(2kR_i + \delta_i(k)) \tag{105}$$

where the index i is for present atomic species i, N is the number of neighbouring atoms, R is the distance to the neighbouring atom, σ is the disorder in the neighbour distance. Because all these parameters are unique informational features of a material, this makes x-ray transmission a powerful method for classification. Additionally, the form $\chi(k)$ is a sum of different x-ray components whose frequency is determined by

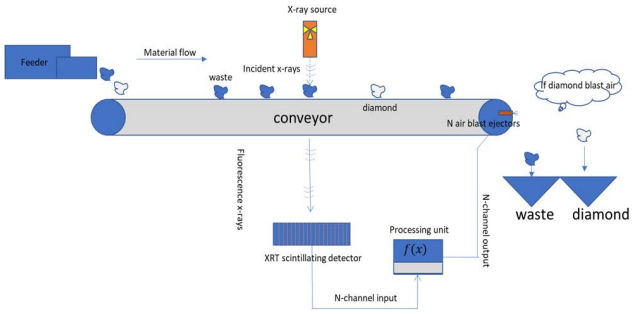

FIGURE 16. X-ray machines in transmission measurement mode.

the argument of the sinusoidal component and the amplitude of each component spectra is a function of the presinusoidal term. Fig. 16 is the configuration of an X-ray machine in transmission measurement mode.

The source x-rays penetrate the sample and are captured by a sensor consisting of scintillating crystals and converted in a current intensity measurement.

The dependence of eqn. 101 on particles size can be eliminated by screening the feed material to a known size range to reduce the number of unknowns to our inversion problem. Depending on the sensing element configurations, the presentation of material into the feeder may or may not require a monolayer on the belt and for particles to be stationary on the belt at the time when they reach the sensing unit. At the sensing unit, which is a line scan camera, the x-rays penetrating the material are converted into a digital image. A calibration exercise is performed with a target sample material and a threshold image with a certain degree of grey is stored for reference [76]. When a particle with relatively the same amount of grey is detected, the control system activates air solenoid valves in the specific channel to cause the material to be ejected into the accept stream, while material with a level of greyness that doesn't conform to the criteria are ignored.

X-ray transmission is very key in dealing with self-absorption phenomena characteristic of x-ray fluorescence when thick samples are inspected but has a poor contrast challenge for thin dilute samples [77]. Self-Absorption is also a high energy phenomenon in fluorescence the signal variation is heavily attenuated at high operating energy [78].

4) COMBINED SORTING MODEL

Thus, with these facts, a new approach is proposed, of combing x-ray transmission measurements with fluorescence measurements. By considering the two extremes, thin dilute sample and thick concentrated sample, we define new measurements based on a combination of x-ray transmission signal and x-ray fluorescence signal

For thin dilute sample

$$\mu_c = I_f/I_o + \ln I_o/I_t = \frac{\epsilon\Delta\Omega}{4\pi}\mu_{xf}(E)\,t + 1 + \mu_{xt}(E)\,t \tag{106}$$

In practical cases, by means of material screening, the value of t is known, making the above equation is a linear combination of the fluorescence and transmission absorption coefficients μ_{xf} and μ_{xt} as per eqn. 18.

For the thick sample case, the combined transmission fluorescence signal is given by

$$\mu_c = I_f/I_o + \ln I_o/I_t = \frac{\epsilon\Delta\Omega}{4\pi k_{f\phi}}\mu_{xf}(E) + \mu_{xt}(E)\,t, \tag{107}$$

since t is a constant or predetermined, again the total signal μ_c is a linear combination of the transmission and fluorescence measurements. The fluorescence and transmission data after edge jump can be approximated by the following six and five parameter models, $[\beta_f\alpha_f\sigma_i r_i\delta_i F]$ and $[\beta_T\alpha_T\sigma_i r_i\delta_i]$ respectively as,

$$\mu_{xf} = (\beta_f + \alpha_f k) + \sum_{i=1}^{N} e^{-k^2\sigma_i^2} sin\ (2kr_i + \delta_i)\, e^{-k^F} \tag{108}$$

And

$$\mu_{xT} = (\beta_T - \alpha_T k) + \sum_{i=1}^{N} e^{-k^2\sigma_i^2} sin\ (2kr_i + \delta_i) \tag{109}$$

where $\beta_f\alpha_f F$ and $\beta_T\alpha_T$ are material properties associated with fluorescence and transmission respectively and σ_i is Debye–Waller factor, r_i is the atomic species radius, δ_i is the scattering phase shift for a particular atomic site. $F > 1$ is the self-absorption exponent associated with fluorescence, which causes the fluorescence amplitude to be more aggressively attenuated at high energies, and $\beta_f + \alpha_f k$ and $\beta_T - \alpha_T k$ are the fluorescent and transmission linear asymptote respectively. Therefore equation (110), as shown at the bottom of the next page.

This form allows for the recovery of high energy signal components from the combined signal, which could otherwise be compromised had a fluorescence mode being considered unaided.

A ratio based contrast formular is not good enough since eqn. 110 has a sinusoidal form and is susceptible to division by zero. A commonly favored approach is a fourier transform based analysis, but since our intention is to define a yes or no criteria for classification and not necessarily involve ourselves with elegent elemental composition analysis, we propose a much simpler method of detection based on the shapes of the combined fluorescence and transmission model. Thus, for two materials including a calibration sample with combined absorption μ_{cs} and an unknown sample μ_{cun}, our approach seeks to determine the similarity between the two shapes of the absorption coefficient graphs. We thus define a new inter-particle contrast through the use of a two sample Kolmogorov-Smirnov test, KS

$$C_{c12} = KS(\mu_{cs}, \mu_{cun}) \tag{111}$$

This function, returns a measure of similarity between any two samples μ_{cs} and μ_{cun} as value between zero and one. The value C_{c12} is generally much different closer to zero for any two dissimilar materials and closer to one for two materials

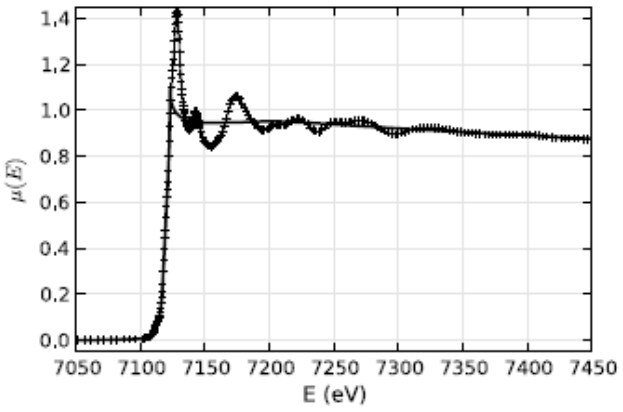

FIGURE 17. FeO X-ray transmission measurement [47].

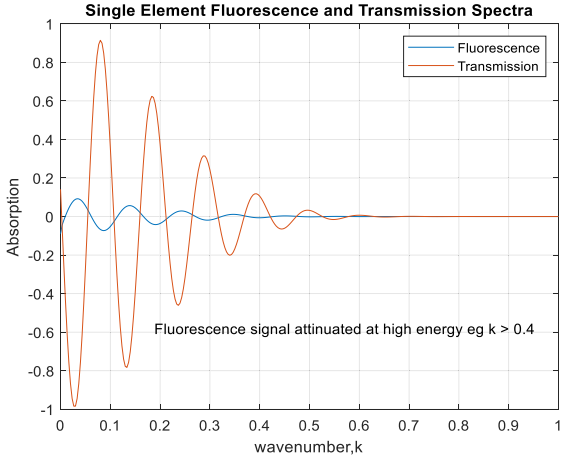

FIGURE 18. Post edge transmission and fluoresence model for random atomic site.

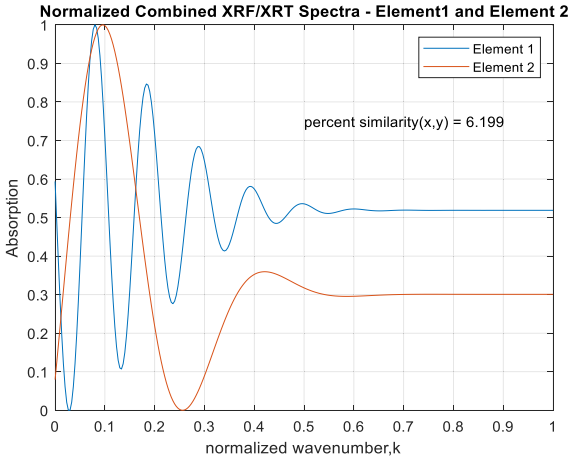

FIGURE 19. Combined transmission and fluoresence model for two dissimilar atoms.

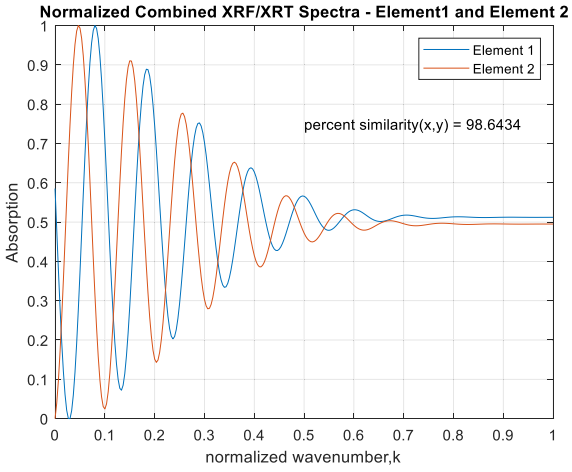

FIGURE 20. Similarity of two similar elements with an small phase distortion due to surface cleanliness or weak impurities.

of the same kind. Based on models six and five parameter models of transmission and fluorescence, we posit to adopt any random values of the set $\{\beta_f \alpha_f \sigma_i r_i \delta_i F\}$ and those of the set $\{\beta_T \alpha_T \sigma_i r_i \delta_i\}$ to represent any atomic species. We claim that this assumption to be valid trick for our simulation and proceed with our investigation.

Fig. 17 is absorption coefficient of FeO [79]. The purpose of Fig. 17 is to support the validity of our claims and our models. The transmission model closely approximates experimental results in Fig. 17, providing confidence that indeed the five and six parameter models are good assumptions.

In Fig 18 are the ideal post edge fluorescence and post edge transmission spectra after removal of post edge line for a pure element. The post edge jump fluorescence signal has acharacteristic attenuation at high energies, while its transmission counterpart, preserves the high energy sinusoids. Figure 19 is the combined spectra of two non-identical elements after post edge line removal. For both spectra, the signal sinusoid are preserved post normalized wavenumber of 0.4, indicating self-absorption mitigation as a results of the transmission mode. For a given calibration element, all other measured signals are compared for similarly using the *KS* test and a decision is made as to the level of similarity. A criterion is then set to determine what level of similarity constitutes a null detection or vice versa. In Fig 19, the similarity between element 1 and element 2 is 9.44%. In figure 20, the inter element similarity is 98.6%.

$$\begin{aligned}\mu_c &= I_f/I_o + \ln I_o/I_t \\ &= \frac{\epsilon \Delta\Omega}{4\pi k_{f\phi}} \left(\left(\beta_f + \alpha_f k\right) + \sum_{i=1}^{N} e^{-k^2\sigma_i^2} \sin\left(2kr_i + \delta_i\right) e^{-k^F} \right) + \left(\left(\beta_T - \alpha_T k\right) + \sum_{i=1}^{N} e^{-k^2\sigma_i^2} \sin\left(2kr_i + \delta_i\right) \right) t \end{aligned} \quad (110)$$

TABLE 2. Qualitative assessment of the electromagnetic sensor-based methods' strengths and limitations.

Influencing Factors	Color sorting	Gamma Sorting	Infra red sorting	X-ray fluorescence	X-ray transmission	Combined X-ray Fluorescence and Transmission
Frequency band	0.4 - 0.7 um	~ 1 pm	750 - 2500 nm	0.01 - 10 nm	0.01 - 10 nm	0.01 - 10 nm
Incident energy intensity	*depends on source brightness*	*Depends on material activity and sample size*	*depends on source intensity*	*depends on source intensity*	*depends on source intensity*	*depends on source intensity*
Reflectance. Properties	*Depends on material illuminated*	*Radiative*	*Transmission*	*Scattering*	*Transmission*	*Transmission*
Line of sight	*Grossly affected by line of sight*	*Independent*	*Independent*	*Independent*	*Independent*	*Independent*
Angle of exit / reflection	*depends on viewing angle*	*Independent*	*Independent*	*depends on incident and exit*	*Independent*	*Independent*
Orientation	*Affected by orientation*	*Independent*	*Independent*	*depends on orientation*	*Independent*	*Independent*
Background lighting or radiation	*Affects signal to noise ratio*	*Other radiations can be easily filtered*	*Affects signal to noise ration*	*Not affected by background*	*not affected by background*	*not affected by background*
Surface roughness	*Affects reflectance properties*	*Independent*	*Independent*	*Independent*	*Independent*	*Independent*
Dimensional limitation	*Independent*	*Dimensionally small active materials may require expensive electronics for detection*	*Useful upto 10 um*	*1 - 32 mm*	*10 - 100 mm*	*1 - 100 mm*
Molecular polarity	*Independent*	*Independent*	*Requires non zero polarity*	*Independent*	*Independent*	*Independent*
Material stiffness	*Independent*	*Independent*	*Low material stiffness may require expensive electronics for detection*	*Independent*	*Independent*	*Independent*
Molecular weight	*Independent*	*Indirectly dependent*	*Independent*	*Independent*	*Independent*	*Independent*
Self Absorption	*None*	*None*	*None*	*Manifests for large sample and high energy*	*None*	*None*
Contrast	*Function of reflecteance*	*None*	*Poor for relatively small materials*	*None*	*Poor for relatively small material*	*Independent*

TABLE 2. ***(Continued.)*** **Qualitative assessment of the electromagnetic sensor-based methods' strengths and limitations.**

Material applicability	*Material with distict level of greyness*	*Detects on the radioactive material*	*very thin polorized materials*	*None*	*None*	*None*
Surface cleanliness	*Affects measurement*	*Independent*	*Affects measurement*	*Independent*	*Independent*	*Independent*
Sub millimeter limitions	*Limited*	*limited*	*applicable*	*None*	*None*	*None*
QUALITATIVE METHOD SCORE	**5/16**	**9/16**	**7/16**	**10/16**	**12/16**	**14/16**

In Fig 20, a deliberate small inpurity was added to pure element model in the form of a phase shift, which may result from weak internal sample inpurity or from noise due an external thin layer over the element of interest. The results show the *KS* method is independent of phase shift.

VI. COMPARISON OF THE DIFFERENT ELECTROMAGNETIC SENSOR-BASED METHODS

Detectors are characterized by their geometry, spatial resolution, conversion gain, quantum interaction efficiency, dynamic range, noise, and linearity of response. For each of the EM sorting methods, each of these performance measures can be, however, impossible to directly compare performances since the responses fall in different regions of the EM spectra. We then compare them based on their useful qualitative assessment of the strengths and limations of the method is articulated in Table 2. With these metrics of comparison, it will then give a picture of the strengths and weaknesses of the sensor-based methods that a designer or user may want to adopt in their application.

VII. CONCLUSION

Sensor based ore sorting is a promising technology for mineral beneficiation, which has the potential to improve thoughput and quality of recovery and thus improving mineral operations bottom line and increasing ore reserves. The sorting applications can range from color sorting, infrared sorting, x-ray sorting and gamma radiation sorting. Each sorting method has key advantages and weakness and has a restricted scope of operation, except for x-ray based methods. A comprehensive survey of the developed ore sorting principles of operation has been pesented. This survey is essential in understanding material and process applications whose discrimination effectiveness can be increased by implementation of a carefully selected sorting criteria. This paper further presented an overview of the up to date x-ray based sorting mechanics of x-ray fluorescence and x-ray transmission as individual independent methods, taking a closer look at the limitation of each singular criteria. A new criteria relying on simultaneous use of x-ray fluorescence and transmissions criteria has been proposed, with promising faster compoutation and throughput as a result of the use of non Fourier transform classification criteria. This method also comitigates the effects of self-absorption in fluorescence and contrast in transmission. The combined x-ray sorting criteria through the use of the proposed Kolomogorov-Smirnov test also proves higher reliability with a similarity of 98.6 % between a dirty sample and calibration model sample. Finally, the combined method offers extensive use cases vis a vis sample features or characteristic as shown in evaluation matrix in Table 2. This survey serves as a guideline for researchers in the area of sensor based sorting in understanding the various available sorting criteria and as a motivation to stimulate non-Fourier based signal processing algorithm in classification with same accuracy but offering better computional time.

REFERENCES

[1] J. Danoczi and A. Koursaris, "Development of luminescent diamond simulants for X-ray recovery," *J. Southern Afr. Inst. Mining Metall.*, vol. 108, pp. 89–97, Feb. 2008.

[2] A. Anupam, S. Bhattacharya, and G. J. de Korte, "Effect of feed size and size distribution on the performance of dense medium cyclones: A critical review," *Int. J. Coal Preparation Utilization*, vol. 40, no. 9, pp. 618–639, Sep. 2020.

[3] E. G. Modise, A. M. Zungeru, J. M. Chuma, S. R. S. Prabaharan, B. Mtengi, A. Ude, and Z. Nedev, "The new paradox of dual modality X-ray diamond sorting," *IEEE Photon. J.*, vol. 13, no. 3, pp. 1–24, Jun. 2021, doi: 10.1109/jphot.2021.3074238.

[4] J. Spooren, "Near-zero-waste processing of low-grade, complex primary ores and secondary raw materials in Europe: Technology development trends," *Resour., Conservation Recycling*, vol. 160, Sep. 2020, Art. no. 104919, doi: 10.1016/j.resconrec.2020.104919.

[5] W. Robben, "Sensor-based ore sorting technology in mining—Past, present and future," *Minerals*, vol. 9, no. 9, p. 523, Aug. 2019, doi: 10.3390/min9090523.

[6] Z. Zhang, Y. Liu, Q. Hu, Z. Zhang, L. Wang, X. Liu, and X. Xia, "Multi-information online detection of coal quality based on machine vision," *Powder Technol.*, vol. 374, pp. 250–262, Sep. 2020, doi: 10.1016/j.powtec.2020.07.040.

[7] I. Silin, K. Hahn, D. Gürsel, D. Kremer, L. Gronen, S. Stopić, B. Friedrich, and H. Wotruba, "Mineral processing and metallurgical treatment of lead vanadate ores," *Minerals*, vol. 10, no. 2, p. 197, Feb. 2020, doi: 10.3390/min10020197.

[8] M. Haas, R. Galler, L. Scibile, and M. Benedikt, "Waste or valuable resource—A critical European review on re-using and managing tunnel excavation material," *Resour., Conservation Recycling*, vol. 162, Nov. 2020, Art. no. 105048, doi: 10.1016/j.resconrec.2020.105048.

[9] Q. Li, W. Zhang, Z. Tang, R. Zhou, J. Yan, C. Zhu, K. Liu, X. Li, and X. Zeng, "Determination of uranium in ores using laser-induced breakdown spectroscopy combined with laser-induced fluorescence," *J. Anal. At. Spectrometry*, vol. 35, no. 3, pp. 626–631, Mar. 2020, doi: 10.1039/c9ja00433e.

[10] A. Zanoletti, A. Cornelio, and E. Bontempi, "A post-pandemic sustainable scenario: What actions can be pursued to increase the raw materials availability?" *Environ. Res.*, vol. 202, Nov. 2021, Art. no. 111681, doi: 10.1016/j.envres.2021.111681.

[11] N. Okada, Y. Maekawa, N. Owada, K. Haga, A. Shibayama, and Y. Kawamura, "Automated identification of mineral types and grain size using hyperspectral imaging and deep learning for mineral processing," *Minerals*, vol. 10, no. 9, p. 809, Sep. 2020, doi: 10.3390/min10090809.

[12] O. Eterigho-Ikelegbe, H. Harrar, and S. Bada, "Rare Earth elements from coal and coal discard—A review," *Minerals Eng.*, vol. 173, Nov. 2021, Art. no. 107187, doi: 10.1016/j.mineng.2021.107187.

[13] C. Hoffmann Sampaio, W. M. Ambrós, B. G. Cazacliu, J. O. Moncunill, M. M. Veras, G. L. Miltzarek, L. F. O. Silva, A. S. Kuerten, and M. A. Liendo, "Construction and demolition waste recycling through conventional jig, air jig, and sensor-based sorting: A comparison," *Minerals*, vol. 11, no. 8, p. 904, Aug. 2021, doi: 10.3390/min11080904.

[14] Y. Ait-Khouia, M. Benzaazoua, and I. Demers, "Environmental desulfurization of mine wastes using various mineral processing techniques: Recent advances and opportunities," *Minerals Eng.*, vol. 174, Dec. 2021, Art. no. 107225, doi: 10.1016/j.mineng.2021.107225.

[15] G. Maier, F. Pfaff, A. Bittner, R. Gruna, B. Noack, H. Kruggel-Emden, U. D. Hanebeck, T. Längle, and J. Beyerer, "Characterizing material flow in sensor-based sorting systems using an instrumented particle," *Automatisierungstechnik*, vol. 68, no. 4, pp. 256–264, Mar. 2020, doi: 10.1515/auto-2019-0128.

[16] N. Meira, M. Silva, R. Oliveira, A. Souza, T. D'Angelo, and C. Vieira, "Edge deep learning applied to granulometric analysis on quasi-particles from the hybrid pelletized sinter (HPS) process," in *Proc. 23rd Int. Conf. Enterprise Inf. Syst.*, 2021, pp. 527–535, doi: 10.5220/0010458805270535.

[17] L. He, S. Wang, Y. Guo, G. Cheng, K. Hu, Y. Zhao, and X. Wang, "Multi-scale coal and gangue dual-energy X-ray image concave point detection and segmentation algorithm," *Measurement*, vol. 196, Jun. 2022, Art. no. 111041, doi: 10.1016/j.measurement.2022.111041.

[18] G. T. Nwaila, H. E. Frimmel, S. E. Zhang, J. E. Bourdeau, L. C. K. Tolmay, R. J. Durrheim, and Y. Ghorbani, "The minerals industry in the era of digital transition: An energy-efficient and environmentally conscious approach," *Resour. Policy*, vol. 78, Sep. 2022, Art. no. 102851, doi: 10.1016/j.resourpol.2022.102851.

[19] I. Silin, Y. Rubinstein, I. Volobayev, A. Liono, D. Gürsel, and H. Wotruba, "Valorisation of abandoned low grade tailings in Albania for recovery of metal concentrates and mineral products," *Russian J. Non-Ferrous Met.*, vol. 62, no. 5, pp. 483–494, Sep. 2021, doi: 10.3103/s106782122105014x.

[20] J. Xing, Z. Zhao, Y. Wang, L. Nie, and X. Du, "Coal and gangue identification method based on the intensity image of lidar and DenseNet," *Appl. Opt.*, vol. 60, no. 22, p. 6566, Jul. 2021, doi: 10.1364/ao.422498.

[21] S. Luukkanen, A. Tanhua, Z. Zhang, R. M. Canales, and I. Auranen, "Towards waterless operations from mine to mill," *Minerals Eng.*, vol. 187, Sep. 2022, Art. no. 107793, doi: 10.1016/j.mineng.2022.107793.

[22] N. Bellusci, P. R. Taylor, D. E. Spiller, and V. Braman, "Coarse beneficiation of trona ore by sensor-based sorting," *Mining, Metall. Explor.*, vol. 39, no. 5, pp. 2179–2185, Aug. 2022, doi: 10.1007/s42461-022-00665-2.

[23] T. Ly, "Zero-field nuclear magnetic resonance of copper minerals," Ph.D. thesis, UNSW Sydney, 2021, pp. 1–133. [Online]. Available: https://physicstoday.scitation.org/doi/10.1063/PT.3.1948, doi: 10.26190/unsworks/22714.

[24] B. Duan, E. R. Bobicki, and S. V. Hum, "Identification of valuable minerals or metals in ores using microwave imaging," *IEEE Trans. Antennas Propag.*, early access, Oct. 3, 2022, doi: 10.1109/tap.2022.3209711.

[25] T. A. Kharlamova, E. I. Khabarova, and Y. Y. Atamanova, "Reagent-free method for extraction of nickel and cobalt from production and washing solutions of ammonia-carbonate oxidative leach," *Mining Inf. Anal. Bull.*, vol. 1, no. 2, pp. 228–240, 2021, doi: 10.25018/0236-1493-2021-21-0-228-240.

[26] M. Kern, J. N. P. Akushika, J. R. A. Godinho, T. Schmiedel, and J. Gutzmer, "Integration of X-ray radiography and automated mineralogy data for the optimization of ore sorting routines," *Minerals Eng.*, vol. 186, Aug. 2022, Art. no. 107739, doi: 10.1016/j.mineng.2022.107739.

[27] N. F. C. de Meira, M. C. Silva, C. B. Vieira, A. Souza, and R. A. R. Oliveira, "Edge deep learning towards the metallurgical industry: Improving the hybrid pelletized sinter (HPS) process," in *Enterprise Information Systems*. Cham, Switzerland: Springer, 2022, pp. 149–167, doi: 10.1007/978-3-031-08965-7_8.

[28] S. Laudari, B. Marks, and P. Rognon, "Classifying grains using behaviour-informed machine learning," *Sci. Rep.*, vol. 12, no. 1, pp. 1–7, Aug. 2022, doi: 10.1038/s41598-022-18250-4.

[29] A. E. M. Safhi, H. Amar, Y. El Berdai, M. El Ghorfi, Y. Taha, R. Hakkou, M. Al-Dahhan, and M. Benzaazoua, "Characterizations and potential recovery pathways of phosphate mines waste rocks," *J. Cleaner Prod.*, vol. 374, Nov. 2022, Art. no. 134034, doi: 10.1016/j.jclepro.2022.134034.

[30] S. C. Chelgani and A. A. Neisiani, "Sensor-based separation," in *Dry Mineral Processing*. Cham, Switzerland: Springer, 2022, pp. 125–148, doi: 10.1007/978-3-030-93750-8_5.

[31] S. Chiong, "Comparison of ore sorting strategies on environmental and economic performance," Honours Thesis, Univ. Queensland Library, Brisbane, QLD, Australia, 2021. [Online]. Available: https://espace.library.uq.edu.au/view/UQ:34ae294, doi: 10.14264/34ae294.

[32] R. Wilson, P. H. J. Mercier, and A. Navarra, "Integrated artificial neural network and discrete event simulation framework for regional development of refractory gold systems," *Mining*, vol. 2, no. 1, pp. 123–154, Mar. 2022, doi: 10.3390/mining2010008.

[33] A. Cardenas-Vera, M. Hesse, R. Möckel, R. G. Merker, T. Heinig, and Q. Van Phan, "Investigation of sensor-based sorting and selective comminution for pre-concentration of an unusual parisite-rich REE ore, South Namxe, Vietnam," *Minerals Eng.*, vol. 177, Feb. 2022, Art. no. 107371, doi: 10.1016/j.mineng.2021.107371.

[34] J. Jin, C.-L. Lin, J. D. Miller, C. Zhao, and T. Li, "X-ray computed tomography evaluation of crushed copper sulfide ore for pre-concentration by ore sorting," *Mining, Metall. Explor.*, vol. 39, no. 1, pp. 13–21, Nov. 2021, doi: 10.1007/s42461-021-00520-w.

[35] B. Duan, E. Bobicki, and S. V. Hum, "Application of microwave imaging in detecting valuable ores," in *Proc. IEEE Int. Symp. Antennas Propag., USNC-URSI Radio Sci. Meeting (APS/URSI)*, Dec. 2021, pp. 1839–1840.

[36] D. Li, X. Huang, H. Ni, and W. Tang, "Research on coal gangue separation method based on dual energy X-ray image technology," in *Proc. 3rd Int. Conf. Electron. Commun.; Netw. Comput. Technol. (ECNCT)*, vol. 12167. SPIE, 2022, pp. 18–23.

[37] H. Harbeck and H. Kroog, "New developments in sensor-based sorting," *Mineral Process.*, vol. 49, no. 5, pp. 4–11, 2008.

[38] N. Rötzer and M. Schmidt, "Decreasing metal ore grades—Is the fear of resource depletion justified?" *Resources*, vol. 7, no. 4, p. 88, Dec. 2018.

[39] R. Knut and O. Karis, "Spectroscopic investigations of electronic structure," in *Advanced Functional Materials* (Science and Technology of Atomic, Molecular, Condensed Matter & Biological Systems), 2012, pp. 45–70.

[40] E. G. D. Santos, R. S. Paranhos, C. O. Petter, A. Young, and M. M. Veras, "Preliminary analysis of the application of sensor based sorting on a limestone mine in the region caçapava do sul, Brazil," in *Proc. 3rd Pan Amer. Mater. Congr. Minerals, Met. Mater.*, 2017, pp. 579–586.

[41] S. Huang, X. Wang, Y. Chen, J. Xu, T. Tang, and B. Mu, "Modeling and quantitative analysis of X-ray transmission and backscatter imaging aimed at security inspection," *Opt. Exp.*, vol. 27, no. 2, p. 337, Jan. 2019.

[42] C. H. Booth and F. Bridges, "Improved self-absorption correction for fluorescence measurements of extended Xray absorption FineStructure," *Phys. Scripta*, vol. 2005, no. T115, p. 202, 2005.

[43] R. M. Trevorah, C. T. Chantler, and M. J. Schalken, "Solving self-absorption in fluorescence," *IUCrJ*, vol. 6, no. 4, pp. 586–602, Jul. 2019.

[44] E. Samei, "Performance of digital radiography detectors: Quantification and assessment methodologies," in *Advances in Digital Radiography*. Oak Brook, IL, USA: Radiological Society of North America, 2003, pp. 37–47.

[45] E. Samei, R. S. Saunders, J. Y. Lo, J. T. Dobbins, J. L. Jesneck, C. E. Floyd, and C. E. Ravin, "Fundamental imaging characteristics of a slot-scan digital chest radiographic system," *Med. Phys.*, vol. 31, no. 9, pp. 2687–2698, Aug. 2004.

[46] E. Samei, J. T. Dobbins, III, N. T. Ranger, and Y. Chen, "Inter-comparison of methods for image quality characterization: 1. Modulation transfer function," *Med. Phys.*, vol. 33, pp. 1454–1465 May 2006.
[47] L. Tröger, D. Arvanitis, K. Baberschke, H. Michaelis, U. Grimm, and E. Zschech, "Full correction of the self-absorption in soft-fluorescence extended X-ray-absorption fine structure," *Phys. Rev. B, Condens. Matter*, vol. 46, no. 6, pp. 3283–3289, Aug. 1992.
[48] A. Alter, "Physical principles of medical imaging by Perry Sprawls," *Med. Phys.*, vol. 15, p. 274, Dec. 1988.
[49] R. Knut and O. Karis, "Spectroscopic investigations of electronic structure," in *Advanced Functional Materials* (Science and Technology of Atomic, Molecular, Condensed Matter & Biological Systems), 2012, pp. 45–70.
[50] A. Gaur and B. D. Shrivastava, "Speciation using X-ray absorption fine structure (XAFS)," *Rev. J. Chem.*, vol. 5, no. 4, pp. 361–398, Oct. 2015.
[51] F. Riedel and M. Dehler, "Recovery of unliberated diamonds by X-ray transmission sorting," *J. Southern Afr. Inst. Mining Metall.*, vol. 110, pp. 193–199, Dec. 2010.
[52] H. Masoumi, S. M. Safavi, and Z. Khani, "Identification and classification of plastic resins using near infrared reflectance spectroscopy," *Int. J. Mech. Mechatron. Eng.*, vol. 2012, no. 6, pp. 877–884, 2012.
[53] V. Allen, J. H. Kalivas, and R. G. Rodriguez, "Post-consumer plastic identification using Raman spectroscopy," *Appl. Spectrosc.*, vol. 53, no. 6, pp. 672–681, Jun. 1999.
[54] J. M. Chalmers and N. J. Everall, *Qualitative and Quantitative Analysis of Plastics, Polymers and Rubbers by Vibrational Spectroscopy*. Hoboken, NJ, USA: Wiley, 2007.
[55] S. M. Safavi, H. Masoumi, S. S. Mirian, and M. Tabrizchi, "Sorting of polypropylene resins by color in MSW using visible reflectance spectroscopy," *Waste Manage.*, vol. 30, no. 11, pp. 2216–2222, Nov. 2010.
[56] S. Brunner, P. Fomin, and C. Kargel, "Automated sorting of polymer flakes: Fluorescence labeling and development of a measurement system prototype," *Waste Manage.*, vol. 38, pp. 49–60, Apr. 2015.
[57] J. M. Anzano, I. B. Gornushkin, B. W. Smith, and J. D. Winefordner, "Laser-induced plasma spectroscopy for plastic identification," *Polym. Eng. Sci.*, vol. 40, no. 11, pp. 2423–2429, Nov. 2000.
[58] H. Yan and H. W. Siesler, "Identification performance of different types of handheld near-infrared (NIR) spectrometers for the recycling of polymer commodities," *Appl. Spectrosc.*, vol. 72, no. 9, pp. 1362–1370, Sep. 2018.
[59] J. Danoczi and A. Koursaris, "Development of luminescent diamond simulants for X-ray recovery," *J. Southern Afr. Inst. Mining Metall.*, vol. 108, pp. 89–97, Jun. 2008.
[60] A. Anupam, S. Bhattacharya, and G. J. de Korte, "Effect of feed size and size distribution on the performance of dense medium cyclones: A critical review," *Int. J. Coal Preparation Utilization*, vol. 40, no. 9, pp. 618–639, Sep. 2020.
[61] B. Akça and S. Z. Erzeneoğlu, "The mass attenuation coefficients, electronic, atomic, and molecular cross sections, effective atomic numbers, and electron densities for compounds of some biomedically important elements at 59.5 keV," *Sci. Technol. Nucl. Installations*, vol. 2014, pp. 1–8, Sep. 2014.
[62] F. Meirer, G. Pepponi, C. Streli, P. Wobrauschek, P. Kregsamer, N. Zoeger, and G. Falkenberg, "Parameter study of self-absorption effects in total reflection X-ray Fluorescence–X-ray absorption near edge structure analysis of arsenic," *Spectrochimica Acta B, At. Spectrosc.*, vol. 63, no. 12, pp. 1496–1502, Dec. 2008.
[63] R. Castañer and C. Prieto, "Fluorescence detection of extended X-ray absorption fine structure in thin films," *J. de Phys.*, vol. 7, no. 2, pp. 337–349, Feb. 1997.
[64] M. R. Robben, H. Knapp, M. Dehler, and H. Wortruba, "X-ray transmission of sorting tungsten ore," *Opt. Characterization Mater.*, pp. 245–258, 2013.
[65] E. Erlich and W. Hausel, *Diamond Deposits: Origin, Exploration, and History of Discovery*. Littleton, CO, USA: SME, 2003, p. 393. [Online]. Available: https://cds.cern.ch/record/1608416
[66] Z. Tan, J. I. Budnick, and S. M. Heald, "Structural parameter determination in fluorescence EXAFS of concentrated samples," *Rev. Sci. Instrum.*, vol. 60, no. 6, pp. 1021–1025, Jun. 1989.
[67] O. Rozenstein, E. Puckrin, and J. Adamowski, "Development of a new approach based on midwave infrared spectroscopy for post-consumer black plastic waste sorting in the recycling industry," *Waste Manage.*, vol. 68, pp. 38–44, Oct. 2017.
[68] M. Benady and G. Miles, "Locating melons for robotic harvesting using structured light," Paper-Amer. Soc. Agricult. Eng., USA, Tech. Rep. 92-7021, 1992.
[69] F. Buemi, M. Massa, and G. Sandini, "Agrobot: A robotic system for greenhouse operations," in *Proc. 4th Workshop Robot. Agricult.*, Toulouse, France, 1995, pp. 172–184.
[70] R. Ceres, J. L. Pons, A. R. Jiménez, J. M. Martín, and L. Calderón, "Design and implementation of an aided fruit-harvesting robot (Agribot)," *Ind. Robot, Int. J.*, vol. 25, no. 5, pp. 337–346, Oct. 1998.
[71] J. Als-Nielsen and D. McMorrow, *Elements of Modern X-ray Physics*. Hoboken, NJ, USA: Wiley, 2001.
[72] C. H. Booth and F. Bridges, "Improved self-absorption correction for fluorescence measurements of extended X-ray absorption fine-structure," *Phys. Scripta*, vol. 2005, no. T115, p. 202, 2005.
[73] C. H. Booth and F. Bridges, "Improved self-absorption correction for fluorescence measurements of extended X-ray absorption fine-structure," *Phys. Scripta*, vol. 2005, no. T115, p. 202, 2005.
[74] M. Newville, P. Līviņš, Y. Yacoby, J. J. Rehr, and E. A. Stern, "Near-edge X-ray-absorption fine structure of Pb: A comparison of theory and experiment," *Phys. Rev. B, Condens. Matter*, vol. 47, no. 21, pp. 14126–14131, Jun. 1993.
[75] J. H. Hubbell, "Photon mass attenuation and mass energy-absorption coefficients for H, C, N, O, Ar, and seven mixtures from 0.1 keV to 20 MeV," *Radiat. Res.*, vol. 70, no. 1, p. 58, Apr. 1977.
[76] M. Hjelm, B. Norlin, H.-E. Nilsson, C. Fröjdh, and X. Badel, "Monte Carlo simulation of the imaging properties of scintillator-coated X-ray pixel detectors," *Nucl. Instrum. Methods Phys. Res. A, Accel. Spectrom. Detect. Assoc. Equip.*, vol. 509, nos. 1–3, pp. 76–85, Aug. 2003.
[77] Z. W. Di, S. Chen, Y. P. Hong, C. Jacobsen, S. Leyffer, and S. M. Wild, "Joint reconstruction of X-ray fluorescence and transmission tomography," *Opt. Exp.*, vol. 25, no. 12, p. 13107, Jun. 2017.
[78] M. Weiss, "Resource recycling in waste management with X-ray fluorescence," M.S. thesis, Montanuniversität Leoben-Institut für Verfahrenstechnik des Industriellen Umweltschutzes, Leoben, Austria, 2011. [Online]. Available: https://pure.unileoben.ac.at/portal/files/2459623/AC08703426n01vt.pdf
[79] D. K. G. De Boer, "Calculation of X-ray fluorescence intensities from bulk and multilayer samples," *X-Ray Spectrometry*, vol. 19, no. 3, pp. 145–154, Jun. 1990.
[80] M. D. de Jonge and S. Vogt, "Hard X-ray fluorescence tomography—An emerging tool for structural visualization," *Current Opinion Struct. Biol.*, vol. 20, no. 5, pp. 606–614, Oct. 2010.
[81] D. C. Konigsberg, B. L. Mojet, G. E. Van Dorssen, and D. E. Ramaker, "XAFS spectroscopy fundamental principles and data analysis," *Topics Catal.*, vol. 10, pp. 143–155, May 2000.
[82] A. Muñoz-Barrutia, C. Pardo-Martin, T. Pengo, and C. Ortiz-de-Solorzano, "Sparse algebraic reconstruction for fluorescence mediated tomography," in *Wavelets XIII*, vol. 7446. SPIE, 2009, pp. 23–32.
[83] Q. Gong, R.-I. Stoian, D. S. Coccarelli, J. A. Greenberg, E. Vera, and M. E. Gehm, "Rapid simulation of X-ray transmission imaging for baggage inspection via GPU-based ray-tracing," *Nucl. Instrum. Methods Phys. Res. B, Beam Interact. Mater. At.*, vol. 415, pp. 100–109, Jan. 2018.
[84] D. B. Petukhova, E. V. Gorbunova, A. N. Chertov, and V. V. Korotaev, "Principles of image processing in machine vision systems for the color analysis of minerals," in *Applications of Digital Image Processing XXXVII*, vol. 9217. SPIE, 2014, pp. 518–527.

ERNEST GOMOLEMO MODISE (Member, IEEE) received the Bachelor of Applied Science degree in electrical engineering from Queen's University, Kingston, ON, Canada, in 2003, the Bachelor of Science degree (Hons.) in mechanics from the University of Pretoria, South Africa, in 2015, and the master's degree in electrical and electronics engineering from the Botswana International University of Science and Technology, Palapye, Botswana, in 2020, where he is currently pursuing the Ph.D. degree with the Electrical, Computer and Telecommunications Department.

ADAMU MURTALA ZUNGERU (Senior Member, IEEE) received the B.Eng., M.Sc., and Ph.D. degrees from the Federal University of Technology, Minna, Nigeria, Ahmadu Bello University, Zaria, Nigeria, and Nottingham University, U.K., respectively. He was a Research Fellow at the Massachusetts Institute of Technology (MIT), USA, where he also obtained a Postgraduate Teaching Certificate, in 2014. He is currently serving as a Professor and the Head of the Department of Electrical, Computer and Telecommunications Engineering, Botswana International University of Science and Technology (BIUST). Before joining BIUST, in 2015, he was a Senior Lecturer and the Head of the Electrical and Electronics Engineering Department, Federal University Oye-Ekiti, Nigeria. He is the Inventor of a termite-hill routing algorithm for wireless sensor networks and three of his patent applications registered with the World Intellectual Property Organization (WIPO). He has also authored five academic books and over 60 international research articles in reputable journals, including the IEEE Systems Journal, IEEE Internet of Things Journal, IEEE Access, and *JNCA* (Elsevier), with over 1000 citations and has an H-Index of 15. He is a registered Engineer with the Council for The Regulation of Engineering in Nigeria (COREN) and a Professional Engineer registered with the Botswana Engineers Registration Board (ERB) and the Association for Computing Machinery (ACM), USA. At present, he is serving as an Associate Editor for IEEE Access journal. He has also served as an International Reviewer to IEEE Transactions on Industrial Informatics, IEEE Sensors Journal, IEEE Access, IEEE Transactions on Mobile Computing, and IEEE Transactions on Sustainable Computing, and *JNCA* (Elsevier). He has also served as the Chairperson for the IEEE Botswana Sub-Section (2019–2020).

BOKANI MTENGI (Member, IEEE) received the Ph.D. degree from Howard University, Washington, DC, USA, in 2015. Her research work in the optimization of optoelectronic materials for quantum computing was in partnership with the Center for Integrated Quantum Materials (CIQM), Harvard University, Boston, MA, USA. She was a Postdoctoral Fellow under the Howard Hughes Medical Institute Microbiology Laboratory, Howard University, as a Transmission Electron Microscopy Imaging Engineer. She worked as a Biomedical Engineer for the Ministry of Health and Wellness, Botswana, for two years. She is currently a Senior Lecturer of electrical and electronics engineering with the Faculty of Engineering, Botswana International University of Science and Technology, where she teaches power systems operation and control and coordinates the Electrical, Computer and Telecommunications Engineering Design Project. Her research interests include power electronics and energy systems. She is the current the Vice-Chairperson for the IEEE Botswana Subsection.

ALBERT UCHENNA UDE received the M.Eng. and Ph.D. degrees in mechanical and materials engineering from the National University of Malaysia, in 2006 and 2011, respectively. He then works as a Senior Researcher for some years after graduation at the Department of Mechanical and Materials Engineering, National University of Malaysia. In 2015, he was appointed as a Senior Lecturer and later the Head of the Department Mechanical Engineering, Papua New Guinea University of Technology. He is currently serving as an Associate Professor at the Botswana International University of Science and Technology (BIUST), Botswana, where he is also the current Research Chairperson of the Advanced Industrial, Materials, Systems (AIMS) Research Group. He has authored two book chapters and many refereed published scholarly/scientific journal articles. His research interests include machine design, PV optimization, materials science, and solid waste.